



Automated segmentation of retinal layers from optical coherence tomography images using geodesic distance



Jinming Duan^{a,*}, Christopher Tench^b, Irene Gottlob^c, Frank Proudlock^c, Li Bai^a

^a School of Computer Science, University of Nottingham, UK

^b School of Medicine, University of Nottingham, UK

^c Ophthalmology Department, University of Leicester, UK

ARTICLE INFO

Article history:

Received 7 September 2016

Revised 9 April 2017

Accepted 2 July 2017

Available online 6 July 2017

Keywords:

Optical coherence tomography

Segmentation

Geodesic distance

Eikonal equation

Partial differential equation

Ordinary differential equation

Fast sweeping

ABSTRACT

Optical coherence tomography (OCT) is a noninvasive imaging technique that can produce images of the eye at the microscopic level. OCT image segmentation to detect retinal layer boundaries is a fundamental procedure for diagnosing and monitoring the progression of retinal and optical nerve diseases. In this paper, we introduce a novel and accurate segmentation method based on geodesic distance for both two and three dimensional OCT images. The geodesic distance is weighted by an exponential function, which takes into account both horizontal and vertical intensity variations in the image. The weighted geodesic distance is efficiently calculated from an Eikonal equation via the fast sweeping method. Segmentation then proceeds by solving an ordinary differential equation of the geodesic distance. The performance of the proposed method is compared with manual segmentation. Extensive experiments demonstrate that the proposed method is robust to complex retinal structures with large curvature variations and irregularities and it outperforms the parametric active contour algorithm as well as graph based approaches for segmenting retinal layers in both healthy and pathological images.

© 2017 Elsevier Ltd. All rights reserved.

1. Introduction

Optical coherence tomography (OCT) is a powerful imaging modality that uses low coherence interferometry to provide high-resolution cross-sectional images of biological tissues, from which structural and molecular information of the tissues can be obtained [1]. Over the past two decades, OCT has become a well-established imaging modality and widely used by ophthalmologists for diagnosis of retinal and optical nerve diseases. One of the OCT imaging biomarkers for retinal and optical nerve disease is the thickness of the retinal layers. Automated OCT image segmentation to detect retinal layer boundaries is therefore required.

However, since the intensity patterns in OCT images are the result of light absorption and scattering in tissues, OCT images usually contain a significant amount of inhomogeneity and speckle noise, posing significant challenges to automated segmentation to identify tissue boundaries and other specific features. With retinal OCT imaging, disrupted retinal structures caused by pathologies and shadows by retinal blood vessels further complicate the segmentation process, leading to inaccuracy or failure of automated retinal layer segmentation algorithms.

In recent years many automatic and semi-automatic OCT segmentation approaches have been proposed. These approaches can be largely divided into three groups: A-scan based methods, B-scan based methods and volume based methods, as illustrated in Fig. 1. A-scan based methods [2–5] detect intensity peak or valley points on the boundaries in each A-scan profile and then connect the detected points to form a continuous boundary using model fitting techniques. These methods can be inefficient and inaccurate. B-scans methods [6–16] outperform A-scan methods in general. However, they are prone to speckle noise in OCT images and likely to fail on pathological images. Common approaches to segmenting two-dimensional (2D) B-scans include active contour methods [6–9,17], shortest-path based graph search [10–12] and statistical shape models [13–15] (i.e., active shape and appearance models [18,19]). Popular volume based methods are graph based [20–26] and pattern recognition methods [27–30]. Computation of these methods can however be very complex and slow. Pattern recognition methods for retinal layer segmentation normally require manually segmented training data for classification. Automated segmentation of retinal layers from OCT images remains a challenge.

In this paper, we present a new algorithm for retinal layer segmentation from OCT images based on a novel geodesic distance weighted by an exponential function. In contrast a single

* Corresponding author.

E-mail address: Jinming.Duan@nottingham.ac.uk (J. Duan).

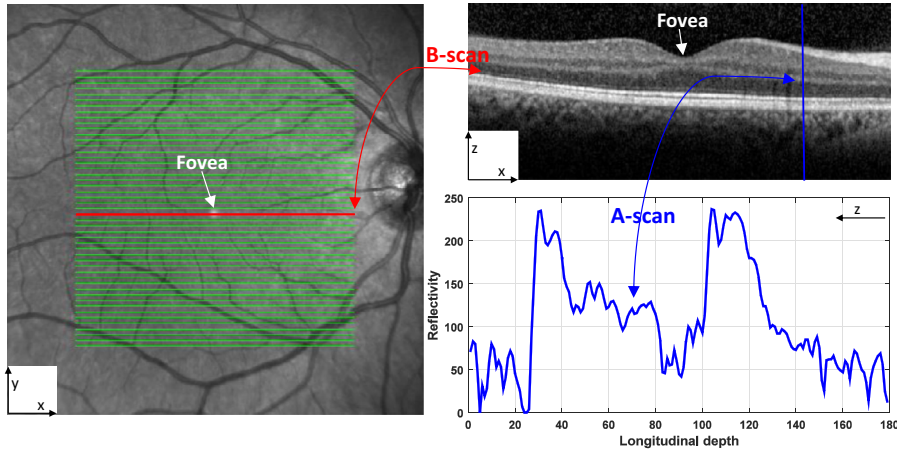


Fig. 1. A en-face fundus image (left) overlaid with lines representing the locations of B-scans in a volumetric OCT image. The red line corresponds to the B-scan in the image (top right). One vertical A-scan of the B-scan is shown in the plot (bottom right). The fovea region is characterised by a depression in the centre of the retinal layer. (For interpretation of the references to colour in this figure legend, the reader is referred to the web version of this article.)

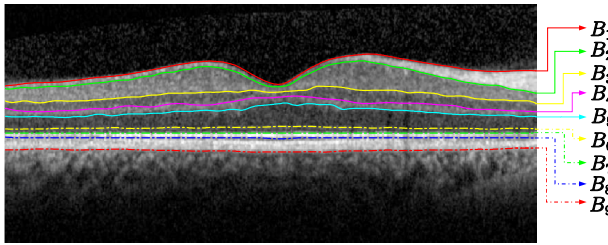


Fig. 2. An example cross-sectional B-Scan OCT image centred at the macula, showing nine target intra-retinal layer boundaries detected by the proposed method. The names of these boundaries labelled as notations B_1, B_2, \dots, B_9 are summarised in Table 1.

horizontal gradient used in other approaches [10,25,26], the exponential function in our method integrates both horizontal and vertical gradient information and can thus account for intensity variations in both directions. The exponential function also plays the role of enhancing weak retinal layer boundaries. As a result, the proposed geodesic distance method (GDM) is able to segment complex retinal structures with large curvatures and other irregularities caused by pathologies. We compute the weighted geodesic distance via an Eikonal equation using the fast sweeping method [31–33]. Retinal layer boundaries can then be detected using the geodesic distance by solving an ordinary differential equation via a time-dependent gradient descent. A local search region is identified based on the detected boundary to detect all the nine retinal layer boundaries and overcome the local minima problem of the GDM. The retinal layer boundaries detected by the proposed GDM are shown in Fig. 2. We evaluate the proposed GDM through extensive numerical experiments and compare it with state-of-the-art OCT segmentation approaches on both healthy and pathological images.

In the following sections, we will first review the state-of-the-art methods for comparison with the proposed GDM, such as parallel double snakes [9], Chiu's graph search [10], Dufour's method [23], and OCTRIMA3D [25,26]. This will be followed by the details of the proposed GDM, ground-truth validation, numerical experiments, and comparison of the GDM with the above mentioned state-of-the-art methods.

2. Literature review

In this section, we will limit our review of the state-of-the-art methods to only those that we will compare our GDM with in Section 3 (i.e., parallel double snakes [9], Chiu's method [10],

OCTRIMA3D [25,26], Dufour's method [23]). For a complete review on related subjects, we refer the reader to [34]. Among the four methods reviewed, the first two are for segmenting 2D B-scans, and the latter two are for segmenting 3D volumes.

Parallel double snakes (PDS): Rossant et al. [9] detected the pathological (retinitis pigmentosa) cellular boundaries in B-scan images by minimising an energy functional that includes two parallel active parametric contours. Their proposed PDS model consists of a centreline $C(s) = (x(s), y(s))$ parametrised by s and two parallel curves $C_1(s) = C(s) + b(s)n(s)$ and $C_2(s) = C(s) - b(s)n(s)$ with $b(s)$ being a spatially varying half-thickness and $n(s) = (n_x(s), n_y(s))$ the normal vector to the centreline $C(s)$. Specifically, their PDS model is defined as

$$E(C, C_1, C_2, b) = E_{\text{Image}}(C_1) + E_{\text{Image}}(C_2) + E_{\text{Int}}(C) + R(C_1, C_2, b), \quad (2.1)$$

where the image energy $E_{\text{Image}}(C_1) = -\int_0^1 |\nabla I(C_1)|^2 ds$ (∇ is the image gradient operator) attracts the parametric curve C_1 towards one of retinal borders of the input B-scan I , whilst $E_{\text{Image}}(C_2)$ handles curve C_2 which is parallel to C_1 . The internal energy $E_{\text{Int}}(C) = \frac{\alpha}{2} \int_0^1 |C_s(s)|^2 ds + \frac{\beta}{2} \int_0^1 |C_{ss}(s)|^2 ds$ imposes both first and second order smooth regularities on the central curve C , with α and β respectively controlling the tension and rigidity of this curve. $R(C_1, C_2, b) = \frac{\varphi}{2} \int_0^1 |b'(C)|^2 ds$ is a parallelism constraint imposed on C_1 and C_2 . Nine retinal borders have been detected by the method, i.e., ILM, RNFL₀, IPL-INL, INL-OPL, OPL-ONL, ONL-IS, IS-OS, OS-RPE and RPE-CH.

Chiu's method: Chiu et al. [10] considered retinal layer boundary detection in a B-scan image as determining the shortest-path that connects two points in a graph $G = (V, E)$, where V is the set of nodes in the graph corresponding to pixels in the B-scan image, and E is the set of weights assigned to pairs of nodes in the graph. Each node is connected only to its eight nearest neighbours, resulting in a sparse adjacency matrix of weights representing intensity variations in vertical direction. For example, an $M \times N$ sized image has an $MN \times MN$ sized adjacency matrix with $8MN$ non-zero entries. The weights are calculated from the intensity gradient of the image in vertical direction. Mathematically, the weights are calculated as

$$w(a, b) = \begin{cases} 2 - (g_a + g_b) + w_{\min} & \text{if } |a - b| \leq \sqrt{2}, \\ 0 & \text{otherwise,} \end{cases} \quad (2.2)$$

where g is the vertical gradient of the B-scan image; a and b denote two separate nodes in V respectively and w_{\min} is a small

Table 1
Notations for nine retinal layer boundaries, their corresponding names and abbreviations.

Notation	Name of retinal layer boundary	Abbreviation
B_1	Internal limiting membrane	ILM
B_2	Outer boundary of the retinal nerve fibre layer	RNFL _o
B_3	Inner plexiform layer-inner nuclear layer	IPL-INL
B_4	Inner nuclear layer-outer plexiform layer	INL-OPL
B_5	Outer plexiform layer-outer nuclear layer	OPL-ONL
B_6	Outer nuclear layer-inner segments of photoreceptors	ONL-IS
B_7	Inner segments of photoreceptors-outer segments of photoreceptors	IS-OS
B_8	Outer segments of photoreceptors-retinal pigment epithelium	OS-RPE
B_9	Retinal pigment epithelium-choroid	RPE-CH

Table 2

Target boundaries of the five methods compared in this paper (check mark means the layer boundary can be detected, while cross mark means the boundary cannot be detected).

Method	ILM (B_1)	RNFL _o (B_2)	IPL-INL (B_3)	INL-OPL (B_4)	OPL-ONL (B_5)	ONL-IS (B_6)	IS-OS (B_7)	OS-RPE (B_8)	RPE-CH (B_9)
PDS [9]	✓	✓	✓	✓	✓	✓	✓	✓	✓
Chiu's method [10]	✓	✓	✓	✓	✓	✗	✓	✗	✓
Dufour's method [23]	✓	✓	✓	✗	✓	✗	✓	✗	✓
OCTRIMA3D [25,26]	✓	✓	✓	✓	✓	✗	✓	✓	✓
Proposed GDM	✓	✓	✓	✓	✓	✓	✓	✓	✓

positive value to stabilise the system. The most prominent layer boundary is then detected as the minimal weighed path from the first to the last vertex in V using the Dijkstra's algorithm. A similar region refinement technique to Section 3.4 was used to detect seven retinal boundaries, i.e., ILM, RNFL_o, IPL-INL, INL-OPL, OPL-ONL, IS-OS and RPE-CH.

Dufour's method: Dufour et al. [23] proposed a modification of optimal graph search approach [35] to segment retinal layers in 3D OCT images. By using soft constraints and prior knowledge, they improve the accuracy and robustness of the original framework. Specifically, their Markov random field based model is given by

$$E(S) = \sum_{i=1}^n (E_{\text{boundary}}(S_i) + E_{\text{smooth}}(S_i)) + \sum_{i=1}^{n-1} \sum_{j=i+1}^n E_{\text{inter}}(S_i, S_j),$$

where S is a set of layer boundaries S_1 to S_n . The external surface energy $E_{\text{boundary}}(S_i)$ is computed from 3D OCT images. The surface smoothness energy $E_{\text{smooth}}(S_i)$ guarantees the connectivity and regularises the layers. The interaction energy $E_{\text{inter}}(S_i, S_j)$ integrates soft constraints to regularise the distances between two simultaneously segmented layer boundaries. This model is then built from training datasets consisting of fovea-centered OCT slice stacks. Their method is capable to segment six retinal layers ($n = 6$ in above formulation) in both healthy and macular edema subjects, i.e., ILM, RNFL_o, IPL-INL, OPL-ONL, IS-OS and RPE-CH.

OCTRIMA3D: Tian et al. [25,26] proposed a real-time automatic segmentation method for 3D OCT images. The segmentation was done frame-by-frame in each 2D B-Scan by considering the spatial dependency between each two adjacent frames. Their work is based on Chiu's graph search framework [10] for B-Scan OCT images, with added inter-frame flattening to reduce the curvature in the fovea region and thus improving the accuracy. They also use inter-frame or intra-frame information to limit the search region in current or adjacent frame so as to increase the computational speed. The method can segment eight retinal layers, i.e., ILM, RNFL_o, IPL-INL, INL-OPL, OPL-ONL, IS-OS, OS-RPE and RPE-CH. Table 2 reports the retinal boundaries detected by the four methods as well as our GDM method detailed in the next section.

3. Proposed geodesic distance method

In this section, we present our GDM method for segmentation of OCT images to detect nine retinal layers defined in Fig. 2 and

Table 1. We will describe the method for 2D segmentation in detail. For 3D segmentation, we first calculate the 3D geodesic distance volume in a manner similar to that of 2D segmentation, followed by minimal path detection on each slice of the geodesic distance volume. In Appendix, we present the implementation details of geodesic distance calculation for both 2D and 3D segmentation.

3.1. Geodesic distance

We use geodesic distance to identify the pixels on the boundaries of retinal layers in OCT images. The geodesic distance d is the smallest integral of a weight function W over all possible paths from two points s_1 and s_2 . The weight function determines how the path goes from s_1 to s_2 . Small weight at one point indicates that the path has high possibility of passing that point. Specifically, the weighted geodesic distance between two endpoints s_1 and s_2 is given by

$$D(s_1, s_2) = \min_C \int_0^1 W^{-1}(C(s)) ds. \quad (3.1)$$

Above $C(s)$ is the set of all possible paths that link s_1 to s_2 , the path length is normalised to unity, and the start and end locations are $C(0) = s_1$ and $C(1) = s_2$, respectively. The infinitesimal contour length ds is weighted by a non-negative function $W(C(s))$. This minimisation problem can be interpreted as finding a geodesic curve (i.e., a path with the smallest weighted length) in a Riemannian space. It is known that the solution of (3.1) satisfies the Eikonal Eq. (3.3).

The retinal layer boundaries in OCT images are normally near horizontal so the largest intensity changes at the layer boundaries are likely to be in the vertical direction. The gradient in the vertical direction is thus taken to compute weight W in (3.1) in order to determine the path that passes the points with maximum gradient changes. For instance, each of the two prominent boundaries, e.g., ILM (B_1) and IS-OS (B_7) in Fig. 3(a) and (e), is at the border of a dark layer above a bright layer. As a result, pixels in the region around the two boundaries have high gradient values, as shown in Fig. 3(b) and (f). As the retinal layers at each side of the boundary are either transiting from dark to bright or bright to dark, the non-negative weight function W in this paper is defined based on

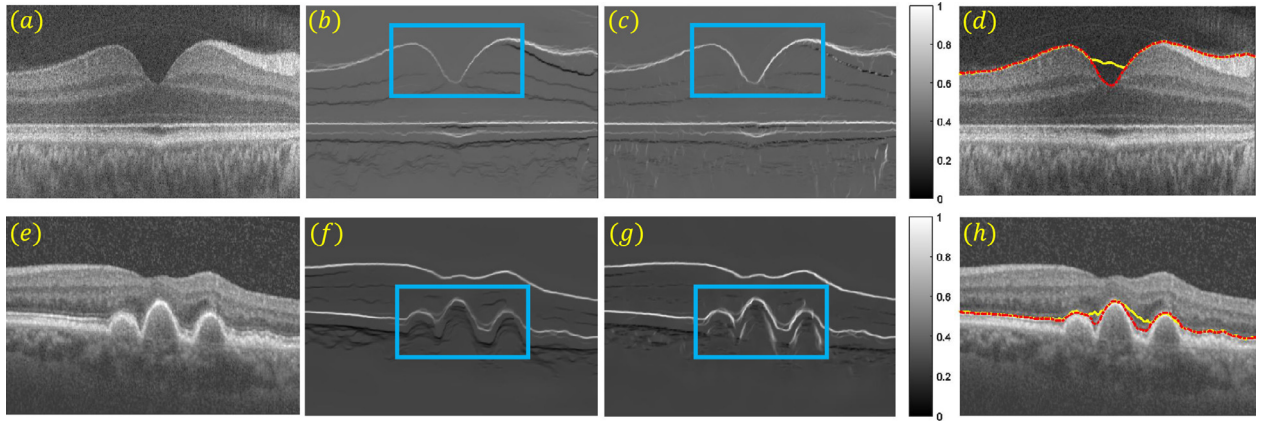


Fig. 3. Effectiveness of the weight W defined in (3.2) on real OCT images. (a) and (e): normal B-scan OCT data and pathological B-scan from an eye with age-related macular degeneration (drye-AMD); (b) and (f): vertical dark-to-bright gradient maps of (a) and (e), respectively; (c) and (g): dark-to-bright gradient maps calculated using Eq. (3.2) with $\lambda = 1$. Note that the pixel gradients have been enhanced in the blue rectangular region where large curvature and bumps occur; (d) and (h): layer boundary detection results using the method described in Section 3.3 with different gradient maps: the yellow lines are computed using (b) and (f), and the red lines using (c) and (g). (For interpretation of the references to colour in this figure legend, the reader is referred to the web version of this article.)

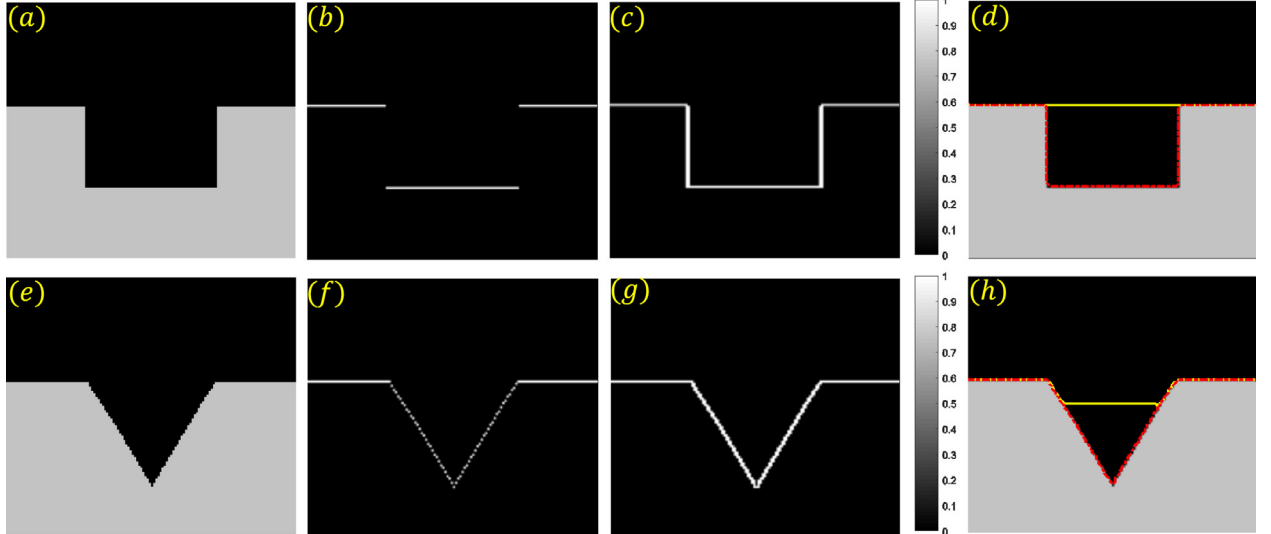


Fig. 4. Effectiveness of the weight W defined in (3.2) on two synthetic images. (a) and (e): synthetic images with changes in both vertical and horizontal directions; (b) and (f): pure vertical dark-to-bright gradient maps of (a) and (e), respectively; (c) and (g): dark-to-bright gradient maps calculated using Eq. (3.2) with $\lambda = 1$ – both vertical and horizontal gradients are enhanced using the proposed method, leading to robust gradient maps for segmentation; (d) and (h): boundary detection via the method described in Section 3.3 using different gradient weights. Yellow lines are computed using (b) and (f), whilst red lines using (c) and (g). (For interpretation of the references to colour in this figure legend, the reader is referred to the web version of this article.)

intensity variation as follows

$$W(x) = \begin{cases} 1 - \exp(-\lambda(1 - n(\nabla_x I))n(|\nabla_y I|)) & \text{dark-to-bright} \\ \exp(-\lambda(1 - n(\nabla_x I))n(|\nabla_y I|)) & \text{bright-to-dark} \end{cases} \quad (3.2)$$

where I is an input OCT image; $n(\cdot)$ is a linear stretch operator used to normalise values to between 0 and 1; \exp is the exponential function, and λ is a user-defined parameter, which together enhance the foveal depression regions and highlight the weak boundaries [36]; ∇_x and ∇_y are the first-order gradient operator along x (vertical) and y (horizontal) direction respectively, which are discretised using a central finite difference scheme under the Neumann boundary condition; and $n(|\nabla_y I|)$ is positive horizontal gradient, without which only vertical direction is accounted for and is thus only applicable to flat boundaries, as evident in Fig. 4. Consequently, the GDM with the weight W defined in (3.2) is robust against curved features (e.g., the central region of the fovea) as well as other irregularities (e.g., bumps or large vari-

ations of boundary locations) caused by pathologies, as illustrated in Fig. 3 as well as in the experimental section.

3.2. Selection of endpoints s_1 and s_2

For fully automated segmentation, it is essential to find a way to initialise the two endpoints s_1 and s_2 automatically. Since the retinal boundaries in the OCT images used in this paper run across the entire width of the image, we add an additional column on each side to the gradient map computed from (3.2). As the minimal weighted path is sought after, a weight W_{\max} larger than any of the non-negative weights calculated from (3.2) is therefore assigned to each of the newly added vertical columns (note that we use W^{-1} for the geodesic distance (3.1), the minimal weighted path thereby prefers large weights). This forces the path traversal in the same direction as the newly added vertical columns with maximal weights, and also allows the start and end points to be arbitrarily assigned in the two columns. Once the retinal layer boundary is detected, the two additional columns can be removed.

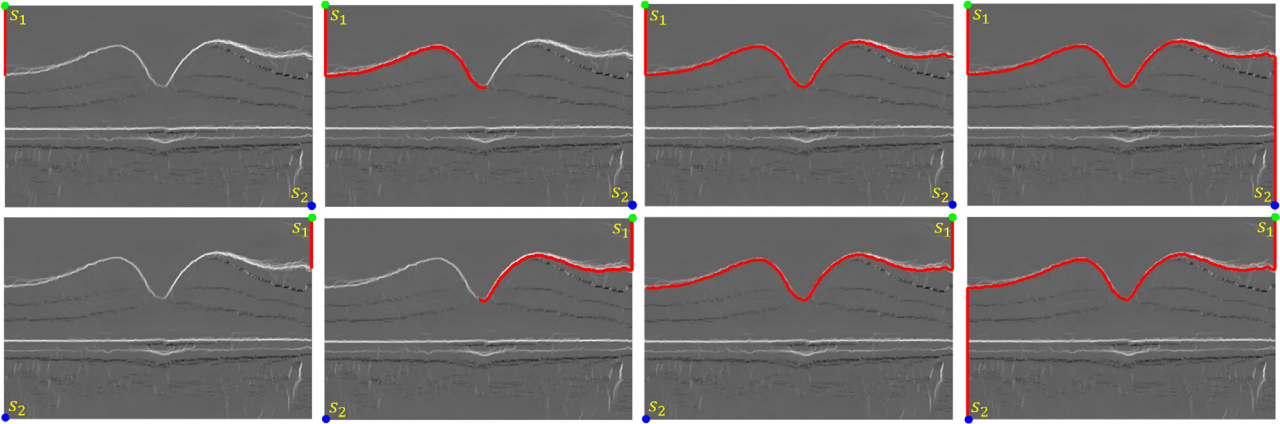


Fig. 5. Two set of segmentation examples using different automatic endpoints initialisations on a dark-to-bright gradient map. s_1 and s_2 are start and end points, respectively. Rows 1 and 2 respectively show the path evolution results using Eq. (3.5). The paths start at s_1 and end at s_2 .

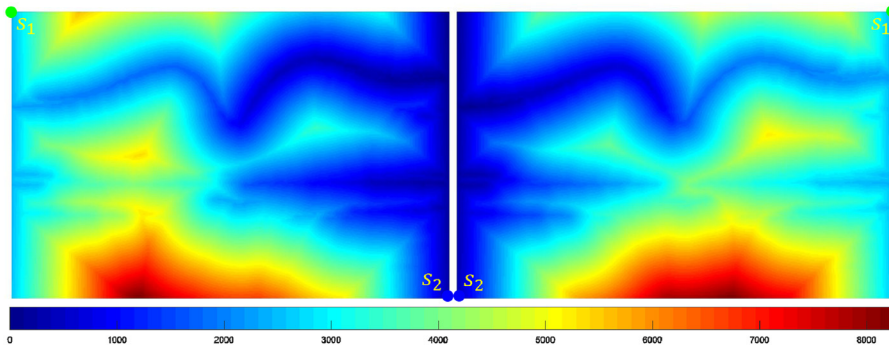


Fig. 6. Distance maps calculated using the fast sweeping method on the gradient weights in Fig. 5. The left distance map is computed using the end point s_2 in the 1st row of Fig. 5, while the right distance map using the end point s_2 in the 2nd row of Fig. 5. The range of distance values is represented by the color bar at the bottom.

Rows 1 and 2 in Fig. 5 respectively show different initialisations of two endpoints as well as the corresponding path evolution results.

3.3. Eikonal equation and minimal weighted path

The solution of (3.1) can be obtained by solving the Eikonal equation after the endpoints are determined. Specifically, over a continuous domain, the distance map $D(x)$ to the seed point s_2 is the unique solution of the following Eikonal equation in the viscosity sense

$$|\nabla D(x)| = W^{-1}(x), \quad x \in \Omega \setminus \{s_2\} \quad (3.3)$$

and

$$D(x) = 0, \quad x \in \{s_2\}.$$

The equation is a first order nonlinear partial differential equation and its solution can be found via the classical fast marching algorithm [37,38] using an upwind finite difference approximation with the computational complexity $O(MN \log(MN))$ (MN is the total number of grid points). Recently, the fast sweeping algorithm [31,32] has been proposed. This technique is based on a pre-defined sweep strategy, replacing the heap priority queue to find the next point to process, and thereby has the linear complexity of $O(MN)$. Fast sweeping is faster than fast marching for simple geometry problems. However, the situation may be reversed for complex geometry. In this paper, we apply fast sweeping for (3.3) and its detailed implementation has been given in Appendix. Fig. 6 shows two distance maps calculated using the weight and end points defined in Fig. 5.

Once the geodesic distance map to the end point s_2 is found, the minimal weighted path (geodesic curve γ) between point s_1

and s_2 can be extracted from the following ordinary differential

Algorithm 1 Proposed GDM for one retinal boundary detection.

- 1: Input OCT B-scan data I
 - 2: Calculate dark-to-bright or bright-to-dark weight W using (3.2)
 - 3: Pad two new columns to the weight and assign large values to them
 - 4: Select two endpoints s_1 and s_2 on the two newly padded columns
 - 5: Calculate distance map D in (3.3) using fast sweeping algorithm
 - 6: Find one retinal layer boundary γ using the gradient descent flow (3.5)
 - 7: Remove the additional columns in the edge detection result
-

equation through the time-dependent gradient descent

$$\gamma'(t) = -\eta_t \nabla D(\gamma(t)), \quad \gamma(0) = s_1, \quad (3.4)$$

where $\eta_t > 0$ controls the parametrisation speed of the resulting curve. To obtain unit speed parametrisation, we use $\eta_t = |\nabla D(\gamma(t))|_\varepsilon^{-1}$. Since the distance map D is nonsmooth at point s_2 , a small positive constant ε is added to avoid dividing by zero. Note that γ is guaranteed to end at the point s_2 by solving the ordinary differential equation, because the distance field is monotonically decreasing from s_1 to s_2 , as observed in Fig. 6. This technique can achieve sub-pixel accuracy for the geodesic path even if the grid is discrete.

The geodesic curve is then numerically computed using a discretised gradient descent, which defines a discrete curve

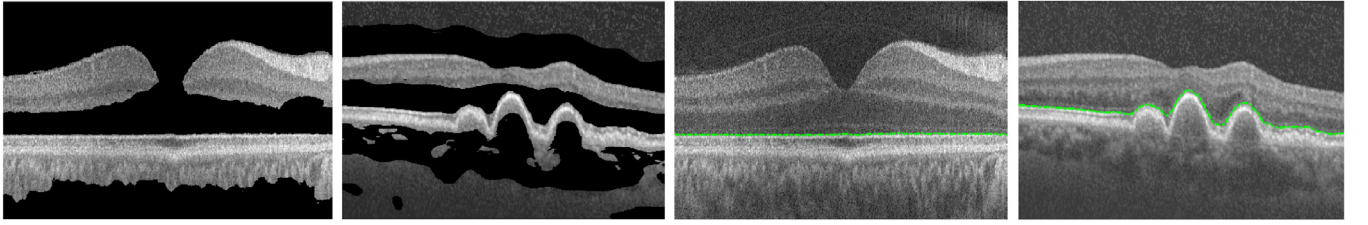


Fig. 7. Detecting the IS-OS boundaries in the normal and pathological images after image enhancement via a local adaptive thresholding method (3.6).

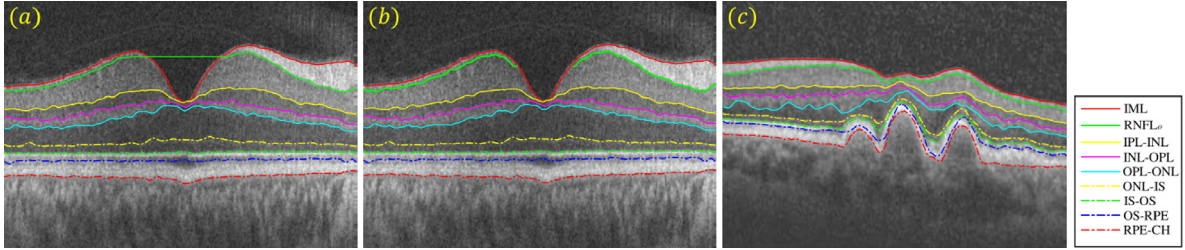


Fig. 8. Segmentation results of the nine retinal layer boundaries on both normal and dye-AMD pathological B-scans, as shown in (a) and (c). The detection of the RNFL boundary however shows errors due to the absence of a search region for this boundary in, as evident in (a). (b) shows that these errors have been corrected.

γ^k using

$$\gamma^{k+1} = \gamma^k - \tau G(\gamma^k), \quad (3.5)$$

where γ^k is a discrete approximation of $\gamma(t)$ at time $t = k\tau$, and the time step size $\tau > 0$ should be small enough. $G(x)$ is the normalised gradient $\nabla D(\gamma(t))/|\nabla D(\gamma(t))|_e$ parametrised by the arc length. Once γ^{k+1} reaches s_2 , one of the retinal boundaries can be found. The following [Algorithm 1](#) concludes the proposed GDM for extracting one retinal boarder from an OCT B-scan.

3.4. Detection of nine retinal layer boundaries

In this section, we show the implementation details of the proposed approach to segment nine retinal layer boundaries, as shown in [Fig. 2](#) and [Table 1](#). Since the proposed model (3.1) is not convex due to the image gradient used, its solution can easily get stuck in local optima. For example, [Fig. 3\(c\)](#) and ([g](#)) have high gradient values in the region around both the ILM and IS-OS boundaries. However, in [Fig. 3\(d\)](#) the algorithm detected the ILM boundary while in [Fig. 3\(h\)](#) it detected IS-OS. In order to eliminate such uncertainty, we dynamically define the search region based on the detected boundaries. The following describes the detection of the nine boundaries in a hierarchical fashion.

3.4.1. Detection of the IS-OS boundary

The intensity variation between two layers divided by the IS-OS (B_7) border are normally the most prominent in OCT B-scans. However, since OCT images are always corrupted by speckle noise as a result of light absorption and scattering in the retinal tissue, it is not always the case. For example, the intensity variation around the IML (B_1) border sometimes can be more obvious than that around IS-OS, as shown in the gradient image [Fig. 3 \(c\)](#). To make sure the first segmentation being the IS-OS boundary we first enhance it via a simple local adaptive thresholding approach,¹ which is given as follows

$$p = \begin{cases} 0 & ls(I, ws) - I > C, \\ 1 & \text{otherwise} \end{cases}, \quad (3.6)$$

where I is the input OCT image, and $ls(p, ws)$ means that I is convolved with a suitable operator, i.e., the mean, Gaussian or median filter. We mention that the purpose of using a filter in (3.6) is

to overcome the inhomogeneity effect by oversmoothing the input image such that the resulting image can be simply segmented by the thresholding method. Our previous research [39,40] has shown that such a method is very robust against intensity inhomogeneity appeared in different medical images. ws is the window size of the filter and C a user-defined threshold value. In the paper, we use the mean filter with window size $ws = 100$ and set $C = 0.01$. The enhanced image can then be obtained by multiplying the original image I with p . The first two images in [Fig. 7](#) illustrate that the contrast of the IS-OS boarder has been enhanced and the most obvious intensity variation now takes place around the IS-OS layer boundary. The IS-OS boundary is then detected on a dark-to-bright gradient image. Consequently, the detected line is guaranteed to pass IS-OS, as shown in the last two images in [Fig. 7](#).

3.4.2. Detection of the RPE-CH, OS-RPE and ONL-IS boundaries

Once IS-OS (B_7) is segmented, it can be used as a reference to limit the search region for segmenting the RPE-CH (B_9), OS-RPE (B_8) and ONL-IS (B_6) boundaries. RPE-CH and OS-RPE are below IS-OS and they are detected in the following way: RPE-CH can be extracted by applying the GDM on the bright-to-dark gradient weight obtained from the region pixels below IS-OS (i.e., the bright-to-dark weight is set to zeros above IS-OS); OS-RPE is then detected on the bright-to-dark gradient weight in the region between the IS-OS and RPE-CH boundaries (i.e., the bright-to-dark gradient weight is set to zeros outside of the region between IS-OS and RPE-CH). ONL-IS is above IS-OS. The search region can be constructed between IS-OS and a parallel line above it with a diameter of 15 pixels. The dark-to-bright gradient weight outside of the region is then set to zeros. Hence, the only layer boundary in the search region is ONL-IS which can be extracted using the GDM on the dark-to-bright gradient weight.

3.4.3. Detection of the ILM and INL-OPL boundaries

Both ILM (B_1) and INL-OPL (B_4) are at the border of a darker layer above a bright layer. The intensity variation around the IML boundary is much more prominent and thus it is segmented first. The detected ONL-IS boundary is taken as a reference and the dark-to-bright gradient weight below ONL-IS is set to zeros. INL-OPL can be then easily detected on the dark-to-bright gradient weight by simply limiting the search region between ILM and ONL-IS (i.e., the dark-to-bright gradient weight is set to zeros outside of the region between ILM and ONL-IS).

¹ <http://homepages.inf.ed.ac.uk/rbf/HIPR2/adptrsh.htm>

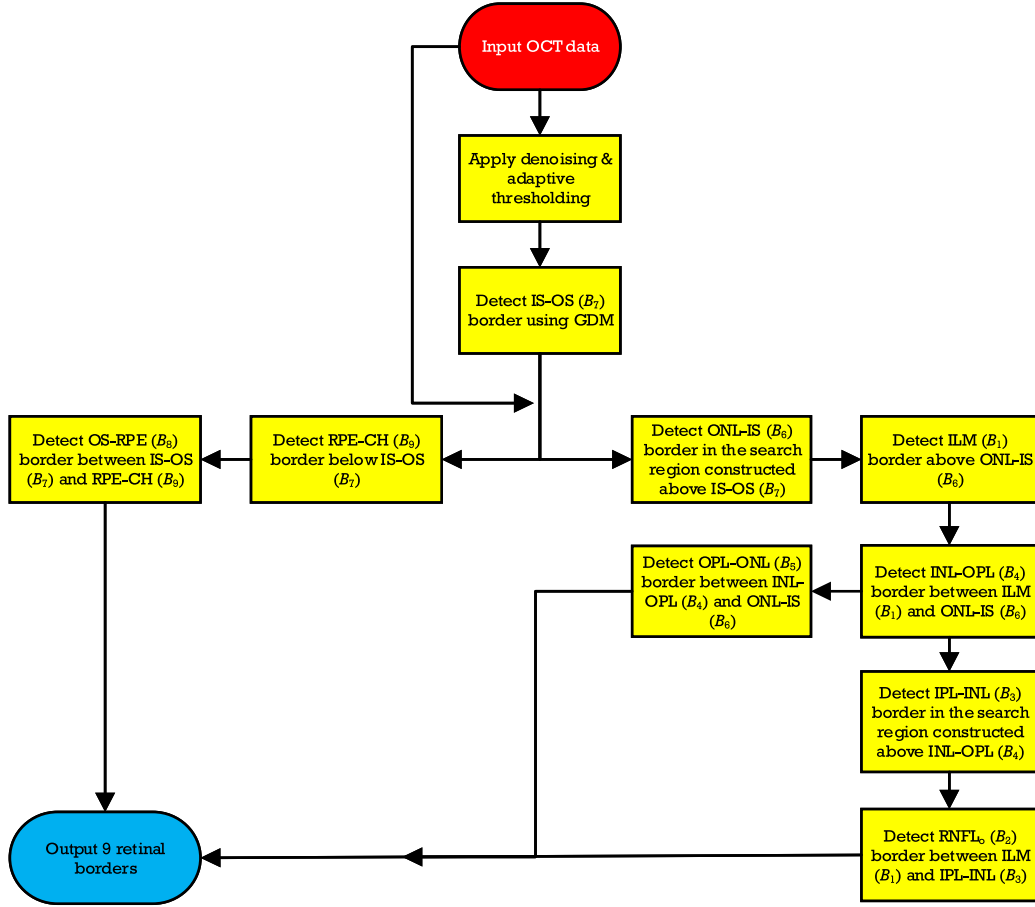


Fig. 9. The overview of the proposed framework for dynamically detecting nine retinal layer boundaries defined in Fig. 2 and Table 1. Section 3.4 describes this flow chart in detail.

3.4.4. Detection of the OPL-ONL, IPL-INL and RNFL_o boundaries

OPL-ONL (B₅), IPL-INL (B₃) and RNFL_o (B₂) demonstrate a bright layer above a darker layer and thus can be detected on the bright-to-dark gradient weight. The segmented INL-OPL and ONL-IS boundaries are taken as two reference boundaries, and OPL-ONL can be found by limiting the search region between INL-OPL and ONL-IS. The search region for IPL-INL can be then constructed between the INL-OPL boundary and a parallel line above it with a diameter of 20 pixels. IPL-INL can be located on a bright-to-dark gradient weight which is set to zeros outside of the search region constructed. Finally, RNFL_o can be found in the search region between the two reference boundaries IPL-INL and IML. However, because the IPL-INL and IML boundaries are very close to each other in the central region of the fovea, the search region for the RNFL_o are sometimes missing around the fovea region. This leads to segmentation errors of RNFL_o, as shown in Fig. 8(a). These errors however can be avoided by simply removing the spurious points detected on RNFL_o in the region above IML, as shown in Fig. 8(b). For clarity, the proposed method for segmenting nine retinal layer boundaries is summarised in the flow chart shown in Fig. 9.

4. Experiment setup

To evaluate the performance of the proposed GDM qualitatively and quantitatively, numerical experiments are conducted to compare it with the state-of-the-art approaches reviewed in Section 2 on both healthy and pathological OCT retinal images. As the GDM is able to segment both 2D and 3D OCT images, we perform numerical experiments on both B-scans and volumetric OCT

images. A pre-processing method [41] is used to reduce noise prior to determining the layers boundaries for all segmentation methods. In the following, we introduce the detailed procedure of OCT data acquisition, evaluation metrics used to quantify segmentation results, final numerical results, and computational complexity of different methods.

4.1. Clinical data

30 Spectralis SDOCT (ENVISU C class 2300, Bioptrigen, axial resolution = 3.3 m, scan depth = 3.4 mm, 32, 000 A-scans per second) B-scans from 15 healthy adults (mean age = 39.8 years, SD = 8.6 years; 7 male, 8 female) were used for the research. All the data was collected after informed consent was obtained and the study adhered to the tenets of the Declaration of Helsinki and Ethics Committee approval was granted.

2D B-scan data: The B-scan was imaged from the left and right eye of 15 healthy adults using a spectral domain OCT device with a chin rest to stabilise the head. The B-scan located at the foveal centre was identified from the lowest point in the foveal pit where the cone outer segments were elongated (indicating cone specialisation). To reduce the speckle noise and enhance the image contrast, every B-scan was the average of aligned images scanned at the same position. In addition to the 30 OCT images from the healthy subjects, another 20 B-scans from subjects with pathologies are also used to compare the proposed GDM with other approaches in pathological cases. These B-scans are from an eye with dry age-related macular degeneration (drye-AMD), which is available from

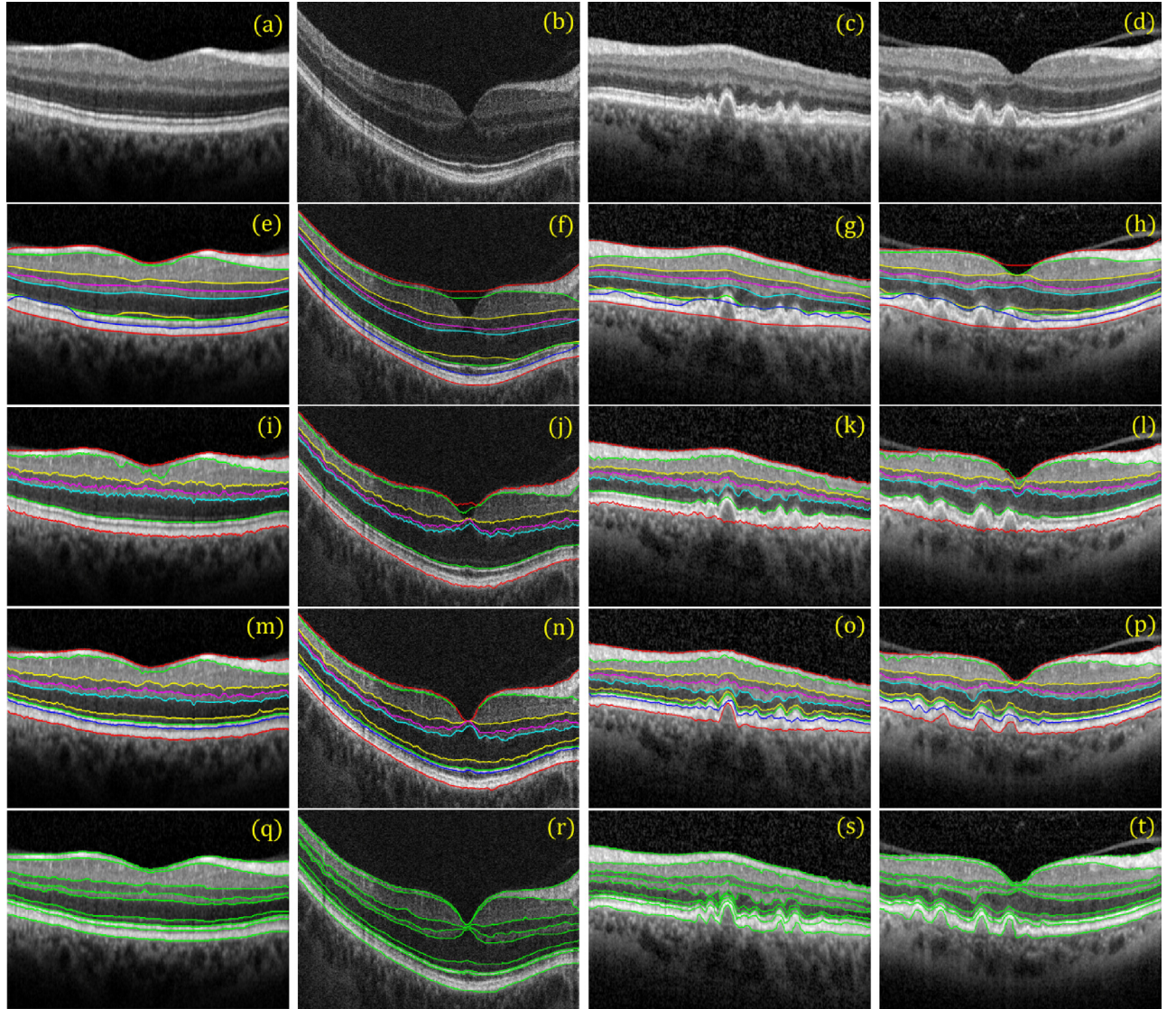


Fig. 10. Comparison of different OCT segmentation methods using healthy and pathological B-scans. 1st row: healthy (i.e., first two) and pathological (i.e., last two) B-scans; 2nd row: results by the PDS model (2.1); 3rd row: results by Chiu's method; 4th row: results by the proposed GDM; 5th row: ground truth.

the Dufour's software package's website.² Segmentation accuracy by the three automated 2D methods (i.e., PDS, Chiu's method and GDM) over these healthy and pathological B-scans is evaluated using the ground truth datasets, which were manually detected with extreme carefulness by one observer.

3D OCT data: 10 Spectralis SD-OCT (Heidelberg Engineering GmbH, Heidelberg, Germany) volume data sets from 10 healthy adult subjects are used in this study. Each volume contains 10 B-scans, and the OCT A-scans outside the 6mm × 6mm (lateral × azimuth) area and centred at the fovea were cropped to remove low signal regions. All volumetric data can be downloaded from [25], where also contains the results of the **OCTRMA3D**, and the manual labellings from two graders. In this study we choose the manual labelling of grader 1 as the 3D ground truth.

4.2. Evaluation metrics

Performance metrics are defined to demonstrate the effectiveness of the proposed GDM and compare it with the existing meth-

ods. Three commonly used measures of success for retinal layer boundary detection are signed error (SE), absolute error (AE) and Hausdorff distance (HD). Among them, SE indicates the bias and variability of the results. AE is the absolute difference between automatic segmentation and ground truth, while HD measures the distance between the farthest point of a set to the nearest point of the other and vice versa. Specifically, these metrics are denoted as

$$SE(B_i, \tilde{B}_i) = \frac{1}{n} \sum_{j=1}^n (B_{ij} - \tilde{B}_{ij}),$$

$$AE(B_i, \tilde{B}_i) = \frac{1}{n} \sum_{j=1}^n (|B_{ij} - \tilde{B}_{ij}|),$$

$$HD(B_i, \tilde{B}_i) = \max \left(\max_{x \in B_i} \left\{ \min_{y \in \tilde{B}_i} \|x - y\| \right\}, \max_{x \in \tilde{B}_i} \left\{ \min_{y \in B_i} \|x - y\| \right\} \right).$$

Above B_i and \tilde{B}_i are respectively the detected boundaries and ground truth boundaries (i.e., manual labellings). n is the number of pixels/volexs that fall on the retinal layer boundary. Statistically, when the SE value is close to zero, the difference between B_i and \tilde{B}_i

² http://pascaldufour.net/Research/software_data.html

Table 3

Mean and standard deviation of SE (μm), AE (μm) and HD (μm) calculated using the results of different methods (PDS, Chiu's method and GDM) and the ground truth manual segmentation, over 30 healthy OCT B-scans. Besides, • (◦) indicates that GDM is better (worse) than the compared methods (paired t -tests at 95% significance level).

Boundary	SE (μm)			AE (μm)			HD (μm)		
	PDS	Chiu et al.	GDM	PDS	Chiu et al.	GDM	PDS	Chiu et al.	GDM
ILM (B_1)	$-3.92 \pm 1.90\bullet$	$-1.22 \pm 0.68\bullet$	0.273 ± 0.33	$4.615 \pm 2.03\bullet$	$2.605 \pm 1.12\bullet$	0.924 ± 0.26	$36.56 \pm 15.9\bullet$	$22.12 \pm 9.23\bullet$	3.702 ± 1.62
RNFL _o (B_2)	$-2.57 \pm 1.38\bullet$	$-1.67 \pm 1.34\bullet$	-0.53 ± 0.37	$3.864 \pm 1.49\bullet$	$2.676 \pm 0.82\bullet$	1.262 ± 0.34	$29.00 \pm 11.6\bullet$	$21.25 \pm 5.98\bullet$	7.340 ± 2.16
IPL-INL (B_3)	$-0.55 \pm 0.83\circ$	$-1.04 \pm 1.21\bullet$	-0.38 ± 0.61	$1.876 \pm 0.60\bullet$	$2.020 \pm 0.79\bullet$	1.314 ± 0.32	$8.619 \pm 3.77\bullet$	$10.53 \pm 5.25\bullet$	7.258 ± 1.92
INL-OPL (B_4)	$0.012 \pm 0.58\bullet$	$-0.90 \pm 0.61\circ$	-0.71 ± 0.71	$1.708 \pm 0.39\circ$	$1.699 \pm 0.40\circ$	1.807 ± 0.51	$6.772 \pm 2.53\circ$	$7.036 \pm 2.84\circ$	7.505 ± 2.96
OPL-ONL (B_5)	$-0.23 \pm 1.29\bullet$	$-1.51 \pm 1.30\bullet$	-1.12 ± 1.17	$2.127 \pm 1.00\bullet$	$2.133 \pm 1.05\bullet$	1.949 ± 0.94	$10.22 \pm 3.70\bullet$	$9.044 \pm 3.48\bullet$	7.463 ± 3.24
ONL-IS (B_6)	$6.010 \pm 0.83\bullet$	–	-0.73 ± 0.49	$6.055 \pm 0.86\bullet$	–	1.376 ± 0.36	$9.969 \pm 1.58\bullet$	–	4.630 ± 1.05
IS-OS (B_7)	$-0.09 \pm 0.61\bullet$	$0.194 \pm 0.49\circ$	0.291 ± 0.63	$0.823 \pm 0.29\bullet$	$0.720 \pm 0.25\circ$	0.771 ± 0.36	$3.676 \pm 1.63\bullet$	$3.240 \pm 1.60\bullet$	2.611 ± 0.74
OS-RPE (B_8)	$5.202 \pm 2.25\bullet$	–	-0.78 ± 0.47	$5.570 \pm 1.76\bullet$	–	1.125 ± 0.36	$8.913 \pm 2.28\bullet$	–	3.601 ± 0.96
RPE-CH (B_9)	$-0.31 \pm 0.79\bullet$	$-0.84 \pm 0.58\bullet$	-0.74 ± 0.69	$1.291 \pm 0.25\bullet$	$1.228 \pm 0.47\bullet$	1.213 ± 0.45	$4.237 \pm 1.47\bullet$	$4.027 \pm 1.31\bullet$	3.831 ± 1.08
Overall	$0.394 \pm 0.39\bullet$	$-1.00 \pm 0.54\bullet$	-0.49 ± 0.23	$3.103 \pm 0.74\bullet$	$1.869 \pm 0.59\bullet$	1.305 ± 0.32	$13.11 \pm 4.25\bullet$	$11.04 \pm 3.75\bullet$	5.327 ± 1.11

Table 4

Mean and standard deviation of SE (μm), AE (μm) and HD (μm) calculated using the results of different methods (PDS, Chiu's method and GDM) and the ground truth manual segmentation, over 20 pathological OCT B-scans. Besides, • (◦) indicates that GDM is better (worse) than the compared methods (paired t -tests at 95% significance level).

Boundary	SE (μm)			AE (μm)			HD (μm)		
	PDS	Chiu et al.	GDM	PDS	Chiu et al.	GDM	PDS	Chiu et al.	GDM
ILM (B_1)	$-0.41 \pm 0.59\bullet$	$-0.34 \pm 0.25\circ$	-0.36 ± 0.29	$0.932 \pm 0.44\bullet$	$0.796 \pm 0.17\bullet$	0.683 ± 0.09	$6.461 \pm 4.86\bullet$	$4.087 \pm 1.01\bullet$	3.337 ± 1.10
RNFL _o (B_2)	$-0.93 \pm 0.93\bullet$	$-0.38 \pm 0.33\bullet$	-0.49 ± 0.50	$1.792 \pm 0.63\bullet$	$1.717 \pm 0.53\bullet$	1.257 ± 0.32	$6.145 \pm 1.84\bullet$	$8.464 \pm 4.55\bullet$	6.109 ± 2.49
IPL-INL (B_3)	$-0.23 \pm 0.62\circ$	$-0.22 \pm 0.27\circ$	-0.32 ± 0.32	$1.228 \pm 0.21\bullet$	$1.149 \pm 0.20\bullet$	0.926 ± 0.16	$7.640 \pm 1.31\bullet$	$5.857 \pm 0.98\bullet$	5.151 ± 1.82
INL-OPL (B_4)	$0.578 \pm 0.64\bullet$	$0.555 \pm 0.39\bullet$	0.392 ± 0.26	$1.546 \pm 0.28\bullet$	$1.563 \pm 0.30\bullet$	1.419 ± 0.16	$7.165 \pm 1.07\bullet$	$8.194 \pm 1.36\bullet$	5.942 ± 1.32
OPL-ONL (B_5)	$-0.04 \pm 1.08\circ$	$0.286 \pm 0.55\bullet$	-0.07 ± 0.64	$2.371 \pm 0.76\bullet$	$2.255 \pm 0.60\bullet$	2.019 ± 0.65	$11.28 \pm 1.95\bullet$	$9.858 \pm 2.76\bullet$	9.281 ± 2.25
ONL-IS (B_6)	$3.339 \pm 1.22\bullet$	–	-0.57 ± 0.72	$4.484 \pm 0.50\bullet$	–	1.442 ± 0.34	$15.23 \pm 4.03\bullet$	–	6.205 ± 1.01
IS-OS (B_7)	$-0.23 \pm 0.86\bullet$	$1.030 \pm 1.06\bullet$	0.350 ± 0.50	$2.415 \pm 1.25\bullet$	$2.399 \pm 1.05\bullet$	1.055 ± 0.22	$15.95 \pm 10.2\bullet$	$17.66 \pm 11.3\bullet$	6.795 ± 4.65
OS-RPE (B_8)	$2.371 \pm 4.17\bullet$	–	0.028 ± 0.41	$5.927 \pm 2.34\bullet$	–	1.821 ± 0.47	$22.63 \pm 12.9\bullet$	–	9.673 ± 1.30
RPE-CH (B_9)	$3.315 \pm 2.59\bullet$	$3.011 \pm 2.98\bullet$	0.027 ± 0.35	$4.797 \pm 2.59\bullet$	$5.146 \pm 2.70\bullet$	2.252 ± 0.46	$31.23 \pm 12.9\bullet$	$32.63 \pm 13.2\bullet$	13.19 ± 3.50
Overall	$0.863 \pm 0.59\bullet$	$0.563 \pm 0.44\bullet$	-0.11 ± 0.22	$2.832 \pm 0.83\bullet$	$2.146 \pm 0.70\bullet$	1.430 ± 0.20	$13.75 \pm 4.72\bullet$	$12.39 \pm 4.06\bullet$	7.300 ± 0.67

is small. In this case, the result is less biased. The measurements of AE and HD (varies from 0 to ∞ theoretically) signify the difference between two boundaries, e.g., 0 indicates that both retinal structures share exactly the same boundary, and larger AE and HD values mean larger distances between the measured boundaries. We also monitor the overall SE (OSE), AE (OAE) and HD (OHD) during all the experiments. They are defined as

$$\begin{aligned} \text{OSE} &= \frac{1}{S} \sum_{i=1}^S \text{SE}(B_i, \tilde{B}_i), \\ \text{OAE} &= \frac{1}{S} \sum_{i=1}^S \text{AE}(B_i, \tilde{B}_i), \\ \text{OHD} &= \frac{1}{S} \sum_{i=1}^S \text{HD}(B_i, \tilde{B}_i). \end{aligned}$$

Here S is the total number of retina boundaries one method can detect.

4.3. Parameter selection

There are five parameters in the PDS model: three smooth parameters α , β , φ and two time step sizes γ_c and γ_b used within the gradient descent equations to minimise the functional (2.1) with respect to C and b . In this paper we use $\alpha = 10$, $\beta = 0$, $\varphi = 700$, $\gamma_c = 10$ and $\gamma_b \geq 2$ suggested in [9]. In addition, as PDS is a nonconvex model and its segmentation results depend on initialisation. We initialise the parallel curves very closely to the true retinal boundaries for fair comparison with other methods. A maximal number of iterations number 500 is used to ensure convergence of the PDS model. The graph theoretic based methods, i.e., Chiu's method, OCTRIMA3D and Dufour's method, require no parameter input. Finally, our GDM has two build-in parameters: λ in

(3.2) and τ in (3.5). We set $\lambda = 10$ and $\tau = 0.8$ to detect the retinal layers in the OCT images.

4.4. Numerical results

We first visually compare the segmentation results of the GDM, PDS and Chiu's graph search method on both healthy and pathological B-scans, which are shown in Fig. 10(a)–(d). The PDS results shown in (e)–(h) have some errors on some of detected boundaries. For instance, the detected B_1 and B_2 boundaries cannot converge to the true retinal boundaries around the central fovea region, as shown in (f) and (h). This is because PDS is the classical nonconvex snake-driven model which has difficulty handling concave boundaries. Moreover, because the B_7 retinal layer has a much stronger image gradient than the B_6 and B_8 layers, some parts of the segmented B_6 and B_8 boundaries have been mistakenly attracted to the B_7 layer. Since Chiu's graph search method merely considers intensity changes in the vertical direction (2.2), it also fails to segment the fovea region layers with strong curvature, as shown in (j) and (l). Moreover, the algorithm cannot handle the irregular bumps caused by pathologies very well, as observed from the bottom B_9 boundaries detected in (k) and (l). In general, Chiu's method works very nicely when retinal structures are flat or smooth without large changes at boundary locations. As compared to the ground truth in the last row, the results by the proposed GDM method are the best, as shown in (m)–(p). As analysed in Section 3, the gradient weights defined in (3.2) account for both vertical and horizontal variations, making it very suitable for both flat and nonflat retinal structures. Hence, GDM is a better clinical tool for detecting retinal layer boundaries from normal and pathological images.

The accuracy of the segmentation results by different methods against ground truth on 30 healthy and 20 pathological B-scans

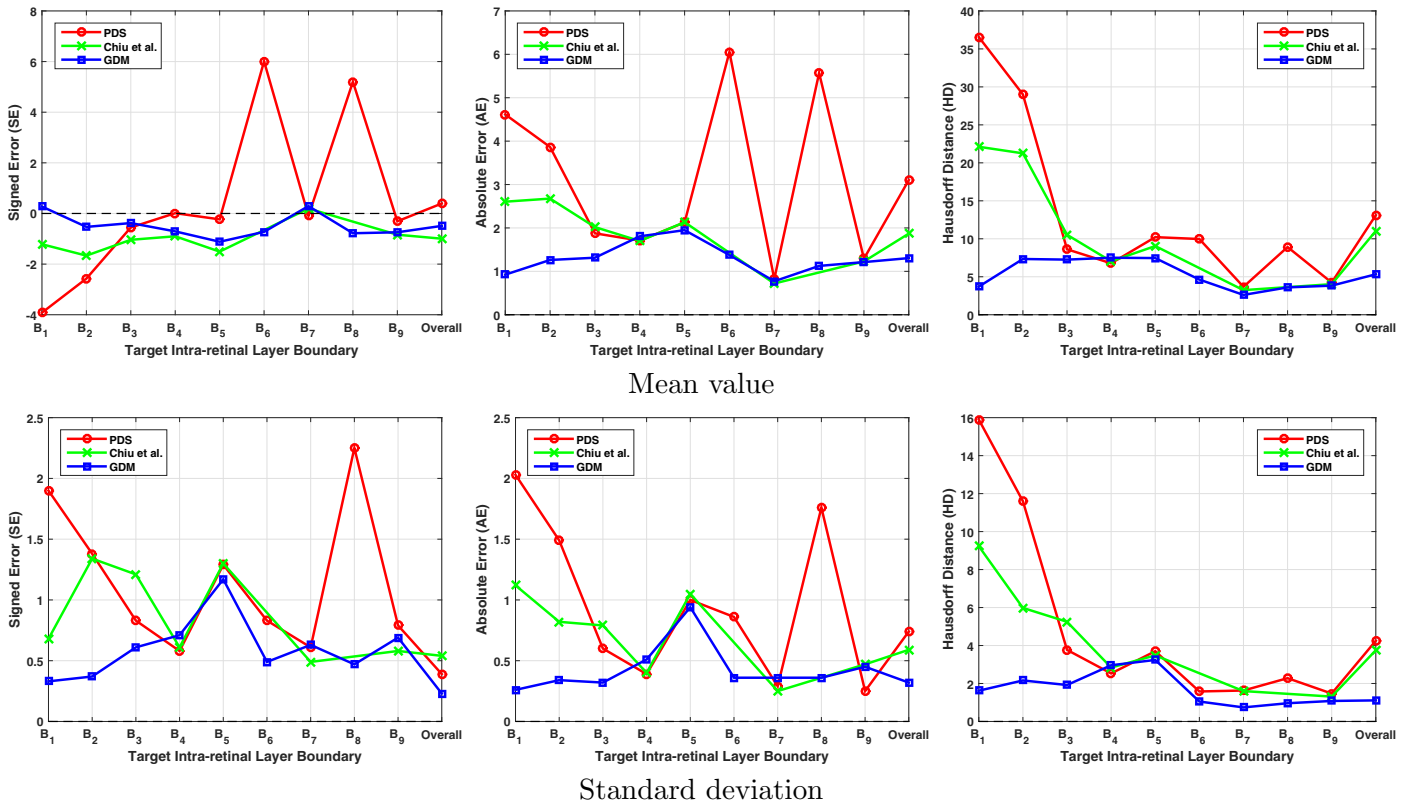


Fig. 11. Plots of mean and standard derivation obtained by different methods in Table 3 for healthy B-scans. The 1st and 2nd rows respectively show the mean and standard derivation of SE (μm), AE (μm) and HD (μm) for segmenting boundaries B_1 – B_9 using PDS, Chiu's method and GDM. The overall value is the average result over all boundaries.

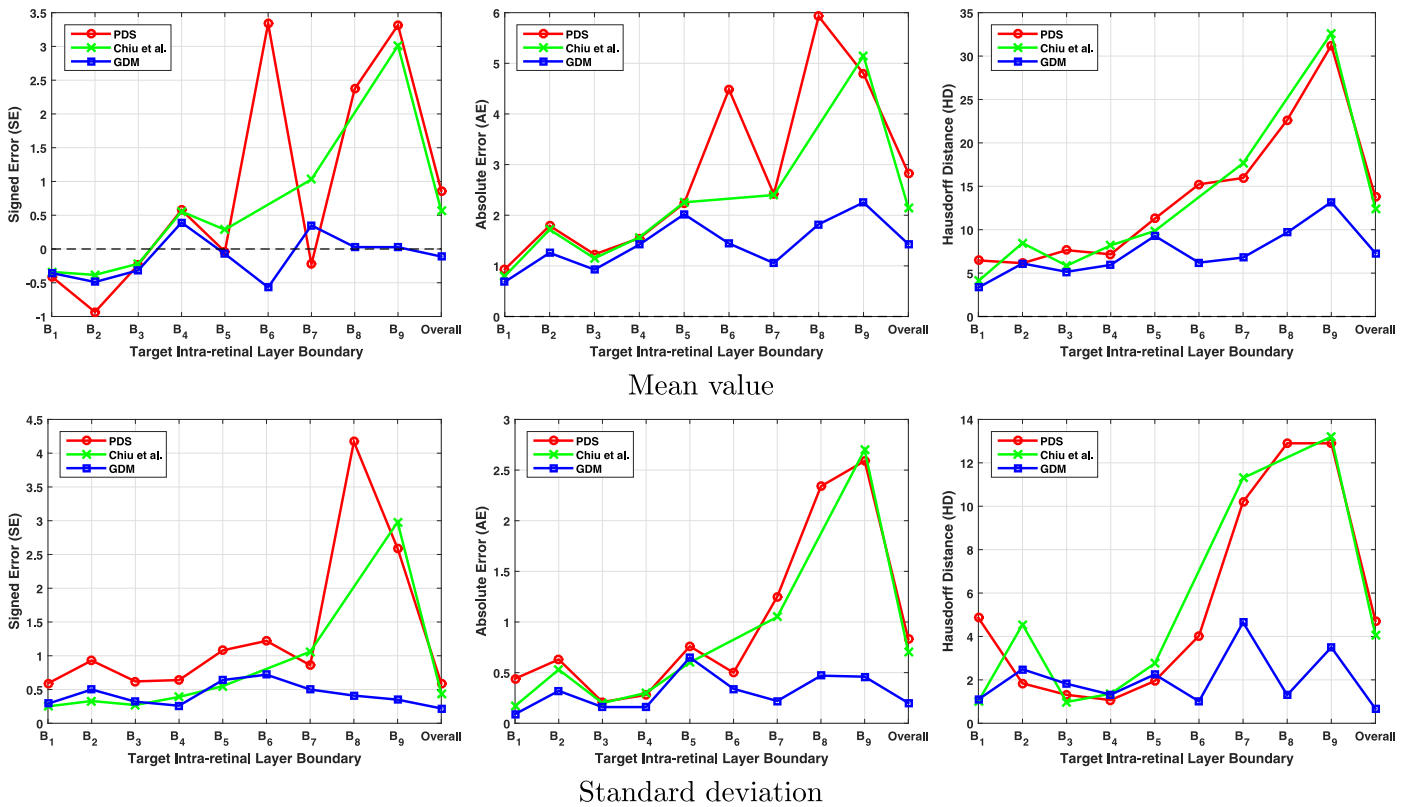


Fig. 12. Plots of mean and standard derivation obtained by different methods in Table 4 for pathological B-scans. The 1st and 2nd rows respectively denote the mean and standard derivation of the SE (μm), AE (μm) and HD (μm) for segmenting boundaries B_1 – B_9 using PDS, Chiu's method and GDM. The overall value is the average result over all boundaries.

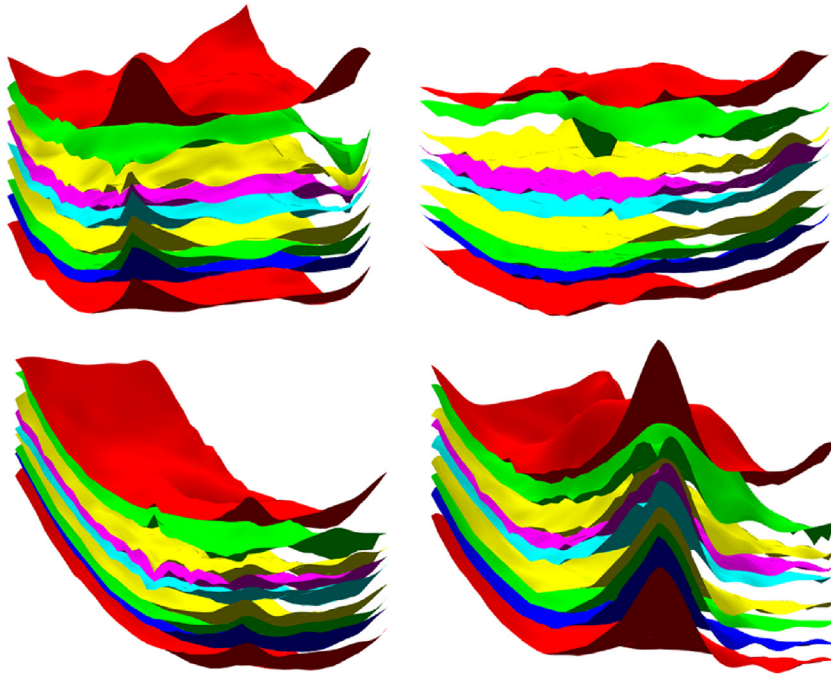


Fig. 13. 3D rendered images of human in vivo intra-retinal layers obtained through segmenting 3D SD-OCT images with the proposed GDM method. Samples are named Volume 1, Volume 2, Volume 7 and Volume 9. The colour used for each individual retinal layer is the same as in Fig. 2.

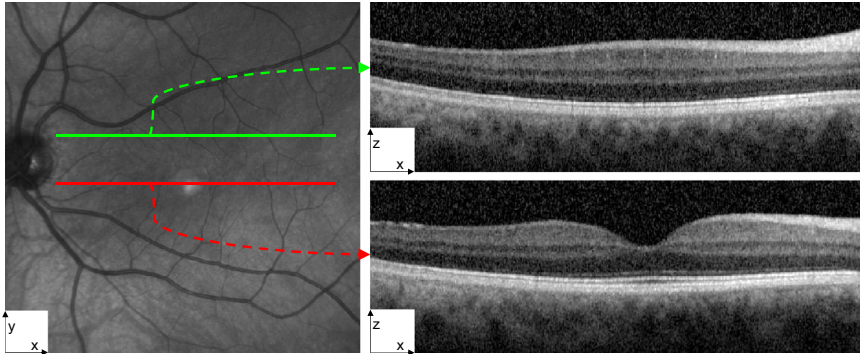


Fig. 14. Two B-scans extracted from Volume 4. The left shows the en-face representation of the OCT scan with the overlaid green and red lines representing the corresponding two B-scans in the right. (For interpretation of the references to colour in this figure legend, the reader is referred to the web version of this article.)

is indicated in Tables 3 and 4, respectively. In order to make the comparison clearer, we plot the data in the tables in Figs. 11 and 12, respectively.

In Table 3 and Fig. 11, the SE values show that PDS leads to large segmentation bias with the largest error being $7.45 \mu\text{m}$, whilst GDM results in small bias with the largest error being $0.92 \mu\text{m}$. The mean SE plot of GDM is close to zero, meaning that GDM is less biased than PDS and Chiu's method. Large errors from PDS normally take place at B_1 , B_2 , B_6 and B_8 , which is consistent with visual inspection on the segmentation results of healthy B-scans in Fig. 10. Furthermore, the AE values show that GDM performs better for most of the segmented boundaries. Particularly at B_1 and B_2 where the curved fovea region is located, the HD values from GDM $\{3.702 \pm 1.62 \mu\text{m}, 7.340 \pm 2.16 \mu\text{m}\}$ are significantly lower than those from PDS $\{36.56 \pm 15.9 \mu\text{m}, 29.00 \pm 11.6 \mu\text{m}\}$ and Chiu's method $\{22.12 \pm 9.23 \mu\text{m}, 21.25 \pm 5.98 \mu\text{m}\}$. However, the accuracy of different methods is comparable at flat or smooth retinal boundaries such as B_4 , B_7 and B_9 . Finally, since the manual segmentation traces small bumps of the true boundaries and the segmentation results by PDS are however very smooth, the overall accuracy of PDS is the lowest among all the approaches compared.

In Table 4 and Fig. 12, we can see that GDM is more accurate and robust compared with the other two methods for pathological data. Larger errors have been found at the last four boundaries B_6 , B_7 , B_8 and B_9 for all the segmentation methods. This is because the dry age-related macular degeneration has led to irregularities to these retinal boundaries, making them less accurate and robust. The overall accuracy measured by the three quantities (SE, AE and HD) has also decreased compared with the counterparts listed in Table 3. Chiu's method using the Dijkstra's algorithm can be deemed as a discrete approximation of the proposed GDM. Therefore, its results are comparable to the GDM results at some flat retinal boundaries while much better than the PDS results. However, the fast sweeping algorithm used to solve the Eikonal equation guarantees local resolution for the geodesic distance, which reduces grid bias significantly and attains sub-pixel accuracy for the geodesic path result from GDM. In addition to the novel weight function proposed in (3.2), GDM also resolves the metrification problem caused by discrete graph methods and thus can achieve more accurate results than Chiu's method.

In the next section, GDM is used to segment OCT volume dataset that includes samples from ten healthy adult subjects, named as Volumes 1–10, respectively. Dufour's method and

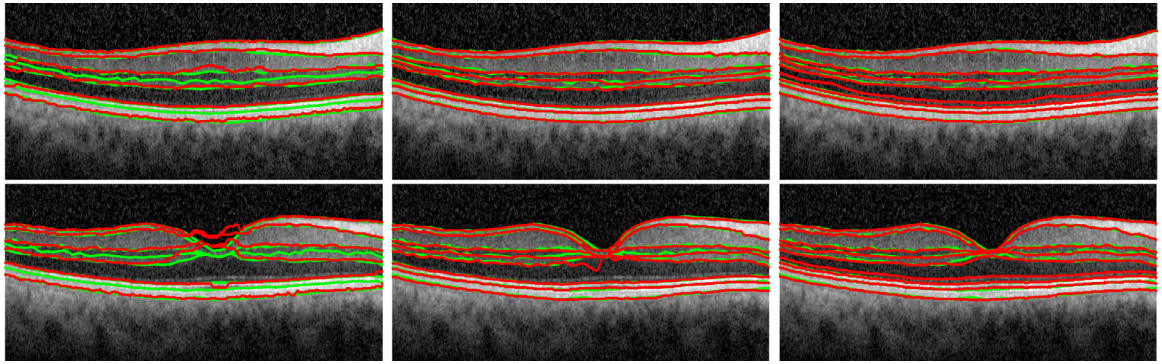


Fig. 15. Comparison between Dufour's method (left), OCTRIMA3D (middle) and GDM (right) on the two B-scans in Fig. 14. The segmentation lines by these methods are marked with red lines while the manual labelled ground truth with green lines. (For interpretation of the references to colour in this figure legend, the reader is referred to the web version of this article.)

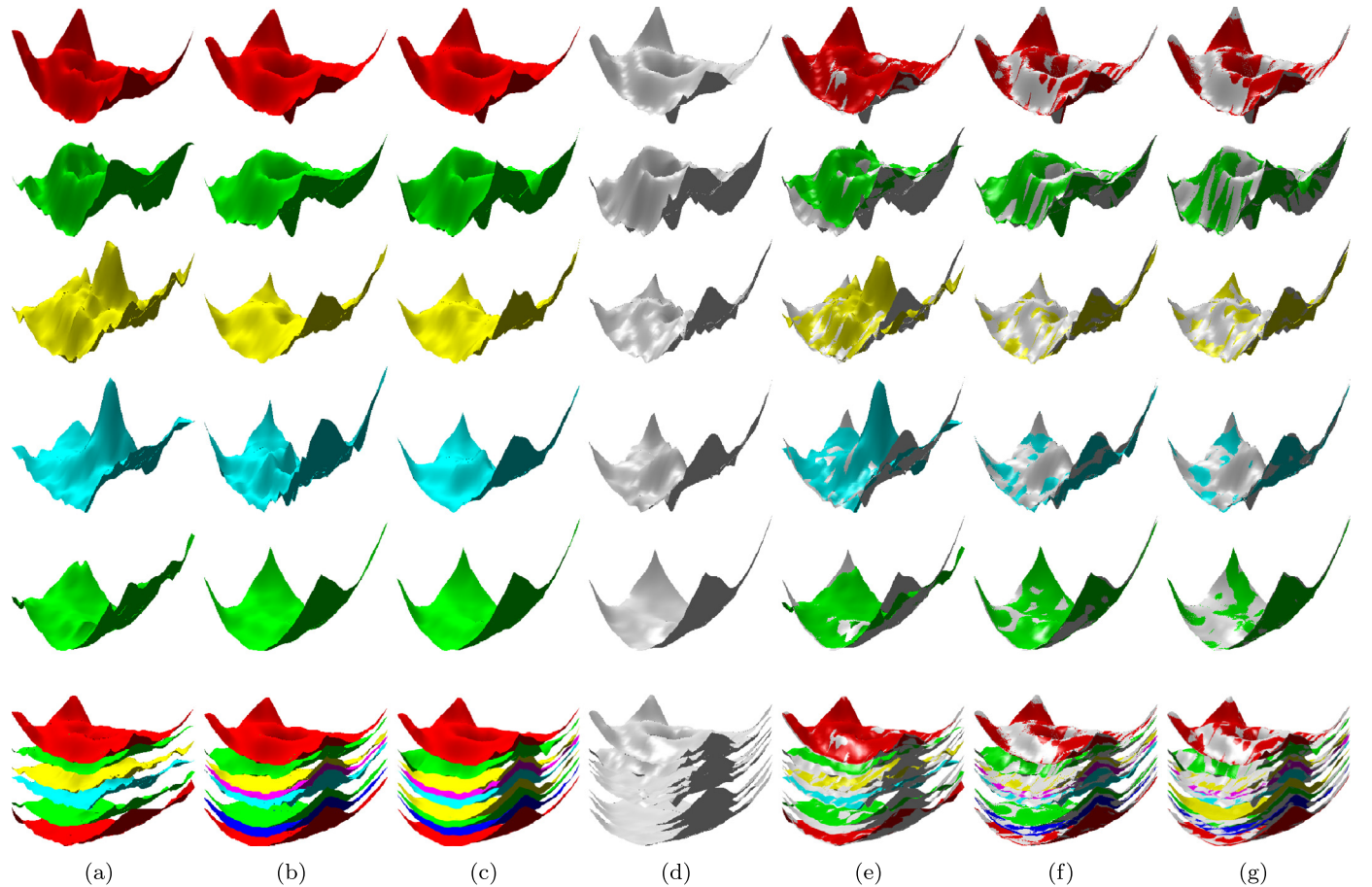


Fig. 16. 3D comparison between Dufour's method, OCTRIMA3D and GDM by segmenting the intra-retinal layers from Volume 4. Column (a)–(d) are respectively Dufour's results, OCTRIMA3D results, GDM results and ground truth. Column (e)–(g) are respectively the segmentation results of the three methods, overlaid with ground truth. Rows 1–6 represent the B_1 , B_2 , B_3 , B_5 , B_7 and overall retinal layer surfaces, respectively.

OCTRIMA3D are also used to segment the same dataset for comparison purposes. In Fig. 13, we demonstrate four representative segmentation results using GDM on Volumes 1, 2, 7 and 9.

Two representative B-scans in Volume 4 are shown in Fig. 14 and their segmentation results by the three approaches are shown in Fig. 15. Note that one B-scan retinal structures are quite flat and the other contains the nonflat fovea region. Dufour's method has lower accuracy than OCTRIMA3D and GDM for both cases. OCTRIMA3D extends Chiu's method to 3D space and improves it by reducing the curvature in the fovea region using the inter-frame flattening technique, so the method performs very

well for both flat and nonflat retinal structures. However, there are still some errors at B_5 . OCTRIMA3D is able to flatten B_1 and in the meanwhile it also increases curvature of its adjacent boundaries such as B_5 , which might be the reason leading to the errors. Compared with the other two, GDM results show less green lines, verifying that the results are closer to ground truth and thus it is the most accurate among the three compared. In addition to the 2D visualisation, the 3D rendering of the results segmented by the three approaches on Volume 4 is given in Fig. 16. The experiment furthermore shows that Dufour's results deviate more from ground truth, while OCTRIMA3D is better than Dufour's method and is

Table 5

Comparison of SE (μm), AE (μm) and HD (μm) calculated using the results of different methods (Dufour's method, OCTRIMA3D and GDM) and manually segmented ground truth, for the OPL-ONL (B_5) layer surface in each of 10 OCT volumes.

Volume #	SE (μm)			AE (μm)			HD (μm)		
	Dufour et al.	OCTRIMA3D	GDM	Dufour et al.	OCTRIMA3D	GDM	Dufour et al.	OCTRIMA3D	GDM
1	-1.194	0.4559	0.3782	2.3816	1.3490	1.0720	25.688	15.273	10.449
2	-2.170	-0.036	-0.128	4.5250	0.9089	0.7814	56.667	11.570	7.0938
3	-2.576	0.4182	0.5983	3.6129	1.3237	1.0989	25.203	16.719	9.5326
4	-2.296	1.0987	0.6774	3.8185	1.5175	1.0753	51.522	18.364	9.6151
5	-1.680	1.3288	0.5909	4.3327	1.5012	0.9005	56.223	11.889	8.8419
6	-2.623	1.0732	0.2974	4.0682	1.4838	0.9493	43.070	19.201	9.5281
7	-2.326	0.5294	0.4529	3.1506	0.9378	0.7433	31.782	8.6701	6.4803
8	-0.636	1.1355	0.6833	2.3955	1.4455	1.0069	25.481	17.930	11.685
9	-4.206	0.3077	0.0859	4.5813	1.0780	0.7678	43.223	8.9694	5.7191
10	-2.648	0.6701	0.2606	4.4903	1.0627	0.7877	41.017	11.666	10.961

Table 6

Comparison of SE (μm), AE (μm) and HD (μm) calculated using the results of different methods (Dufour's method, OCTRIMA3D and GDM) and manually segmented ground truth, for the IS-OS (B_7) layer surface in each of 10 OCT volumes.

Volume #	SE (μm)			AE (μm)			HD (μm)		
	Dufour et al.	OCTRIMA3D	GDM	Dufour et al.	OCTRIMA3D	GDM	Dufour et al.	OCTRIMA3D	GDM
1	-0.432	-0.148	-0.019	1.1013	0.5391	0.4437	16.559	4.7616	4.5805
2	0.7476	-0.276	-0.079	2.0329	0.5539	0.3971	20.309	5.2093	3.7743
3	-0.311	-0.291	-0.106	1.4347	0.5406	0.4629	18.432	2.9790	4.0176
4	0.3652	-0.116	0.3363	1.6954	0.5271	0.4601	27.853	5.3672	2.7882
5	0.6057	-0.098	0.0994	1.7567	0.4756	0.3500	26.556	3.7573	3.4150
6	0.9825	-0.592	-0.139	2.4970	0.7247	0.4066	23.487	5.9301	3.9297
7	-1.247	-0.536	0.0237	1.3895	0.7501	0.3716	10.016	3.1398	3.6980
8	-0.311	-0.069	0.1740	1.0438	0.4053	0.3466	15.044	4.2301	4.3940
9	-0.755	-0.111	0.1407	0.8068	0.5422	0.3939	3.5210	3.4263	3.3868
10	-0.099	-0.220	0.1028	1.2941	0.5609	0.4246	13.313	3.1210	3.5361

Table 7

Comparison of OSE (μm), OAE (μm) and OHD (μm) calculated from the results of different methods (Dufour's method, OCTRIMA3D and GDM) and manually segmented ground truth, for the overall retinal layer surfaces in each of 10 OCT volumes.

Volume #	OSE (μm)			OAE (μm)			OHD (μm)		
	Dufour et al.	OCTRIMA3D	GDM	Dufour et al.	OCTRIMA3D	GDM	Dufour et al.	OCTRIMA3D	GDM
1	-1.271	0.3607	0.4338	1.8358	1.1204	0.9538	17.486	9.3358	7.9163
2	-1.161	0.0246	0.0640	2.5380	0.9652	0.7238	29.682	7.7987	6.1267
3	-1.513	-0.052	0.3456	2.1470	0.9343	0.7838	19.985	8.3491	6.9920
4	-1.431	0.4272	0.3560	2.5278	1.0374	0.8667	31.346	9.4042	7.3130
5	-1.020	0.6369	0.5021	2.4119	1.0794	0.8289	32.607	8.6822	7.1379
6	-1.434	0.4216	0.3969	2.6754	1.1371	0.8606	28.629	9.5267	7.2548
7	-2.010	0.0059	0.3283	2.2458	0.9682	0.7407	21.788	7.0644	6.8279
8	-1.031	0.5815	0.5785	1.7462	1.1063	0.9067	17.610	10.100	8.5112
9	-1.951	0.0542	0.2014	2.1368	0.8771	0.6922	21.344	5.7482	5.4794
10	-1.513	0.1022	0.2109	2.3315	0.8397	0.6596	24.841	6.3250	6.7132

comparable to GDM. GDM results cover less grey ground truth and are the best.

Tables 5–7 contain the quantitative accuracy comparison of the three methods on 10 OCT volumes. Table 5 shows the results for layer boundary B_5 around the fovea region, while Table 6 presents the results for boundary B_7 which is flatter and smoother. In Table 5, the SE values indicate that Dufour's method produces larger segmentation bias than OCTRIMA3D and GDM. The SE values by GDM are in the range of $[-0.128 \mu\text{m} \text{ } 0.6833 \mu\text{m}]$, showing less variability than those by the other two methods. Moreover, GDM leads to the smallest AE and HD values in all 10 cases, indicating that GDM is the most accurate among all the methods. Compared with Table 5, Table 6 shows a significant improvement of all the methods. For example, the range of the HD values by Dufour's method has dropped from $[25.688 \mu\text{m} \text{ } 56.667 \mu\text{m}]$ to $[3.521 \mu\text{m} \text{ } 27.853 \mu\text{m}]$. In addition, the accuracy gap between OCTRIMA3D and GDM has been reduced, and in Volumes 3, 7 and

10 the HD values by OCTRIMA have even become smaller than those by GDM. These improvements are due to the fact that the retinal layer boundary B_7 is flatter and smoother than B_5 . From the values of OAE and OHD in Table 7, we observe that the accuracy of GDM is the highest for the segmentation of total retinal boundaries from each of 10 OCT volumes.

The corresponding boxplots of Tables 5–7 are shown in Fig. 17. These boxplots show that the proposed GDM method performs consistently better, with higher accuracy and lower error rates for both flat and nonflat retina layers. There is little variation in performance across different structures and even in the worst case scenario the proposed method yields lower error rate than the average performance of other methods. In Fig. 18 we present 3D plots of the SE, AE and HD values computed by the three methods on the 10 volumes. For GDM, its SE values are closer to zero and its AE and HD values remain smaller. The overall distribution of these data points also indicates that the GDM results are less oscillating.

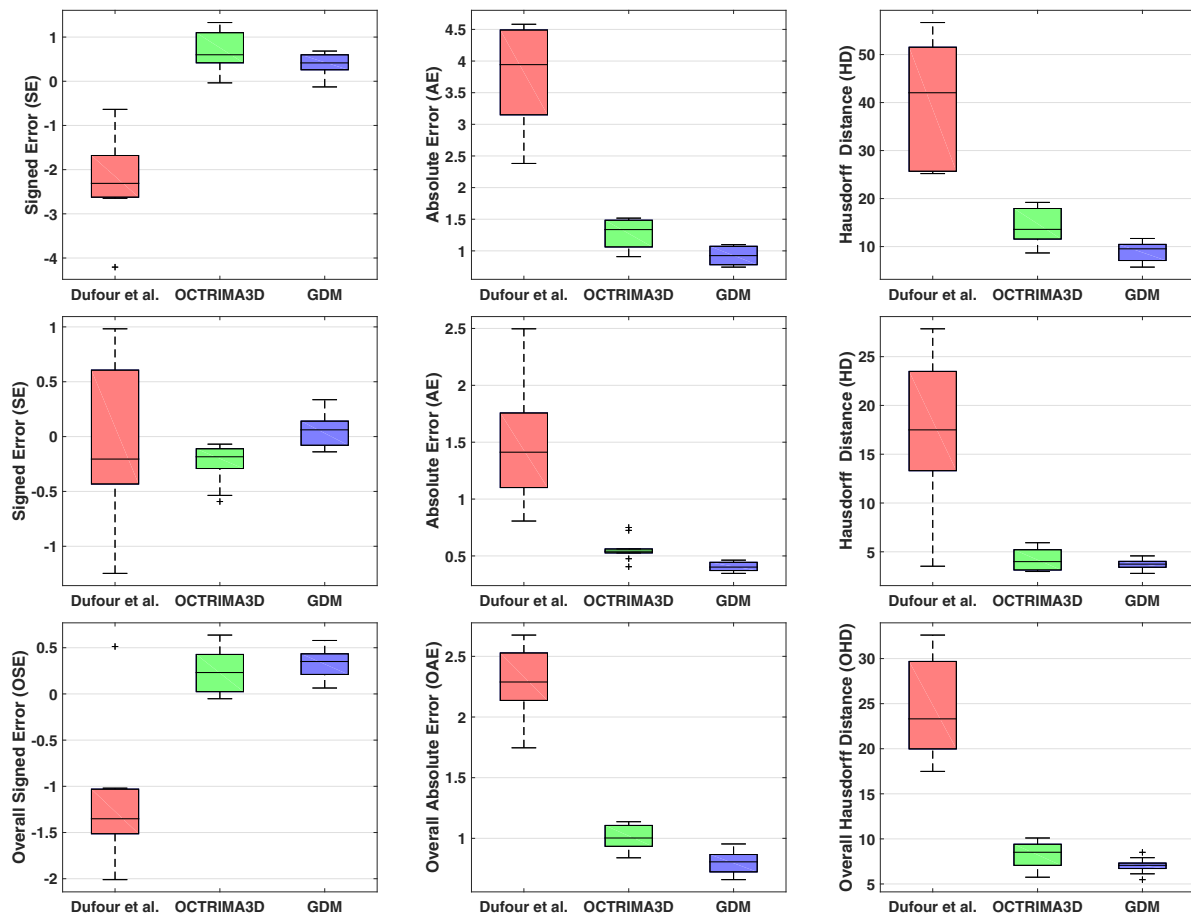


Fig. 17. Boxplots for SE (μm), AE (μm), HD (μm), OSE (μm), OAE (μm) and OHD (μm) obtained by different methods in Tables 5–7 for 10 OCT volumes. 1st row: boxplots of Table 5; 2nd row: boxplots of Table 6; 3rd row: boxplots of Table 7.

We can thus conclude that GDM performs the best among all the methods compared for extracting intra-retinal layer layers from 3D OCT volumes.

4.5. Computation time

In this section, the performance of the different approaches in terms of the computation time is demonstrated. We implemented PDS, Chiu's method and GDM using Matlab 2014b on a Windows 7 platform with an Intel Xeon CPU E5-1620 at 3.70 GHz and 32 GB memory. For a 633×496 sized B-scan, with initialisation close to the true retinal boundaries, it takes 3.625 s (500 iterations) for PDS to detect two parallel boundaries. Chiu's method needs 1.962 s to detect one layer boundary, while GDM only takes 0.415 s. Note that the time complexity of Chiu's graph search method is $O(|E|\log(|V|))$, where $|V|$ and $|E|$ are the number of nodes and edges and $|V| = MN$ and $|E| = 8MN$ in boundary detection in an image. Hence the time complexity of the method is $O(MN\log(MN))$. In contrast, our GDM solved using fast sweeping has linear complexity of $O(MN)$, which is more efficient than Chiu's method. For 3D segmentation, OCTRIMA3D explores spatial dependency between two adjacent B-scans and applies Chiu's method to each 2D slice independently. OCTRIMA3D is thus able to track retinal boundaries in 3D OCT images efficiently. It was reported in [25] that the processing time of the OCTRIMA3D for the whole OCT volume of $496 \times 644 \times 51$ voxels was 26.15 s, which is faster than our GDM (40.25 s is used to segment a $496 \times 633 \times 10$ sized volume). Finally, Dufour's graph method needs 14.68 s to detect the six intra-retinal layer boundaries on a $496 \times 633 \times 10$ sized volume. Dufour's method was im-

plemented using a different programming language (C) and it detected different number of retinal layers from that of GDM, so comparison cannot be made between the two methods.

5. Conclusion

In this paper, we presented a new automated retinal layer segmentation method based on the geodesic distance for both 2D and 3D OCT images. The method integrates horizontal and vertical gradient information and can thus account for intensity changes in the both directions. Furthermore, the exponential weight function employed within the approach enhances the foveal depression regions and weak retinal layer boundaries. As a result, the proposed method is able to segment complex retinal structures with large curvatures and other irregularities caused by pathologies. Extensive numerical results, validated with ground truth, demonstrate the effectiveness of proposed method for segmenting both normal and pathological OCT images. The proposed method has achieved higher segmentation accuracy than the state of the art methods compared, such as the parametrised active contour model and the graph theoretic based approaches. Ongoing research includes integrating the segmentation framework into a system for detection and quantification of retinal fractures and other eye diseases.

Acknowledgement

This research has received funding from the Biotechnology and Biological Sciences Research Council (BBSRC) and Medical

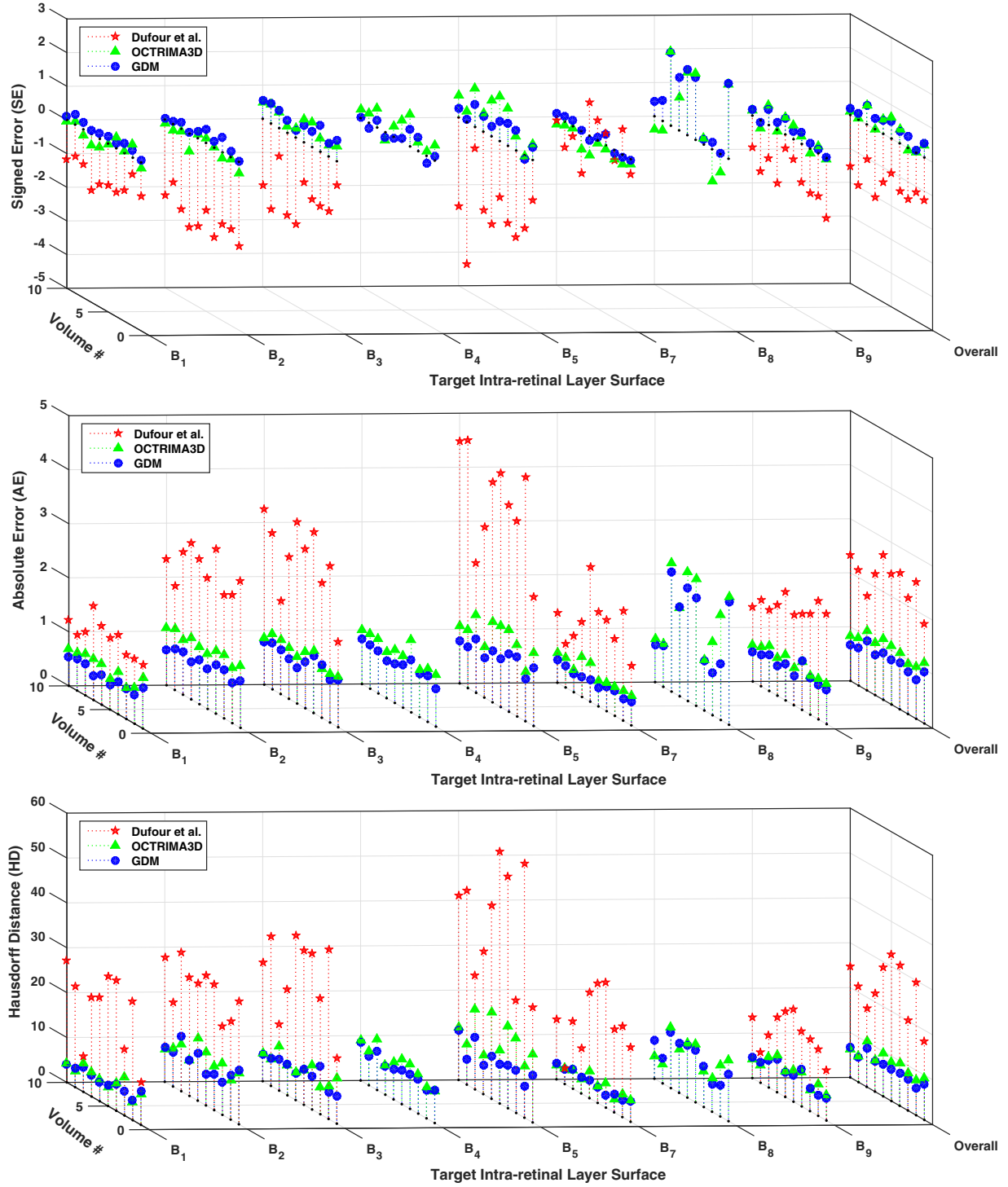


Fig. 18. 3D plots of SE (μm), AE (μm) and HD (μm) obtained using Dufour' method, OCTRIMA3D and GDM on 10 OCT volumes.

Research Council (MRC), under grant agreement numbers P027105 and N004566, respectively.

with

$$d(x) = 0, x \in \Gamma \subset \mathbb{R}^m. \quad (\text{A.2})$$

Above $\Omega \subset \mathbb{R}^2$ and $\Omega \subset \mathbb{R}^3$ respectively correspond to 2D and 3D cases. In OCT segmentation, $\Gamma = \{s_2\}$ where $\{s_2\}$ is a seed point in 2D or multiple seed points in 3D, and $f(x)$ is $W^{-1}(x)$ where the weight function W is defined in (3.2). For 2D implementation, we use x_{ij} to denote a pixel point in the computational domain Ω , and d_{ij} to denote the numerical solution at x_{ij} . For 3D implementation, we use x_{ijk} to denote a voxel point in Ω , and d_{ijk} to denote the

Appendix

We solve the Eikonal equation using the fast sweeping algorithm [31] for OCT segmentation. Consider the following generalised version of the Eikonal equation:

$$|\nabla d(x)| = f(x), x \setminus \Gamma \text{ and } x \in \mathbb{R}^m \quad (\text{A.1})$$

numerical solution at $x_{i,j,k}$. The pixel or voxel size is set to 1 for all the cases.

A1. 2D Implementation

The 2D Godunov upwind difference scheme is used to discretise (A.1) as follows

$$[(d_{i,j}^n - d_{xmin}^n)^+]^2 + [(d_{i,j}^n - d_{ymin}^n)^+]^2 = f_{i,j,k}^2, \quad (\text{A.3})$$

where $d_{xmin}^n = \min(d_{i,j+1}^n, d_{i,j-1}^n)$, $d_{ymin}^n = \min(d_{i+1,j}^n, d_{i-1,j}^n)$ and

$$x^+ = \begin{cases} x & x > 0 \\ 0 & x \leq 0 \end{cases}. \quad (\text{A.4})$$

Boundary conditions need to be handled appropriately for (A.3) in the computational grid space Ω . One-sided upwind difference is used for each of 4 boundaries in the grid space. For example, at the left boundary, a one-sided difference along the x direction is computed as

$$[(d_{i,1}^n - d_{i,2}^n)^+]^2 + [(d_{i,1}^n - d_{ymin}^n)^+]^2 = f_{i,1}^2.$$

If we denote $a = d_{xmin}^n$ and $b = d_{ymin}^n$, numerically solving the Eq. (A.3) with its boundary condition needs to iteratively update

$$d_{i,j}^{n+1} = \min(d_{i,j}^n, \tilde{d}_{i,j}), \quad (\text{A.5})$$

where

$$\tilde{d}_{i,j} = \begin{cases} \min(a, b) + f_{i,j} & |a - b| \geq f_{i,j} \\ \frac{a+b\sqrt{2f_{i,j}^2-(a-b)^2}}{2} & |a - b| < f_{i,j} \end{cases}. \quad (\text{A.6})$$

Initialisation. The hard constraint $d(x) = 0, x \in \Gamma$ in (A.2) should be satisfied over iterations. For initialisation, we assign exact values $d(x) = 0$ for the pixel points on Γ . These values are forced to be zeros at each iteration to satisfy such hard constraint. For the rest of pixel points in Ω , we assign large positive values for $d(x)$. These values will be updated later.

Gauss-Seidel iterations with alternating sweeping orderings. (A.5) is not analytical so iterations are needed to solve it numerically. The Gauss-Seidel iterative method is used here for fast convergence. There are different sweeping schemes that can be applied to Gauss-Seidel, such as the red-black sweeping, Lexicographic ordering sweeping, etc. In [31], the whole domain Ω is swept with the four alternating orderings repeatedly

(1) $i = 1 : M, j = 1 : N$; (2) $i = M : 1, j = N : 1$;

(3) $i = 1 : M, j = N : 1$; (4) $i = M : 1, j = 1 : N$.

Note that for simple geometry of Γ it may be sufficient for (A.5) to converge after applying the sweeping only once. However, for non-uniform problems and/or complex geometry, repeated sweeping might be required in order for (A.5) to converge.

A2. 3D Implementation

The 3D Godunov upwind difference scheme is used to discretise (A.1) as follows

$$[(d_{i,j,k}^n - d_{xmin}^n)^+]^2 + [(d_{i,j,k}^n - d_{ymin}^n)^+]^2 + [(d_{i,j,k}^n - d_{zmin}^n)^+]^2 = f_{i,j,k}^2. \quad (\text{A.7})$$

Above, $d_{xmin}^n = \min(d_{i,j+1,k}^n, d_{i,j-1,k}^n)$, $d_{ymin}^n = \min(d_{i+1,j,k}^n, d_{i-1,j,k}^n)$, $d_{zmin}^n = \min(d_{i,j,k+1}^n, d_{i,j,k-1}^n)$ and x^+ is defined as (A.4). Boundary conditions need to be handled as well in the grid space Ω . One-sided upwind difference is used for each of the 6 boundary faces of the grid space. For example, at the left boundary face, a one-sided difference along the x direction is computed as

$$[(d_{i,1,k}^n - d_{i,2,k}^n)^+]^2 + [(d_{i,1,k}^n - d_{ymin}^n)^+]^2 + [(d_{i,1,k}^n - d_{zmin}^n)^+]^2 = f_{i,1,k}^2.$$

d_{xmin}^n , d_{ymin}^n and d_{zmin}^n are then sorted in an increasing order and the sorted version is recorded as a_1 , a_2 and a_3 . So, the unique solution to (A.7) is given as follows:

$$d_{i,j,k}^{n+1} = \min(d_{i,j,k}^n, \tilde{d}_{i,j,k}), \quad (\text{A.8})$$

where $\tilde{d}_{i,j,k}$ is a piecewise function containing three parts

$$\tilde{d}_{i,j,k} = \begin{cases} \frac{1}{3}(a_1 + a_2 + a_3) \\ + \sqrt{3f_{i,j,k}^2 - (a_1 - a_2)^2 - (a_1 - a_3)^2 - (a_2 - a_3)^2} \\ \frac{1}{2}(a_1 + a_2 + \sqrt{2f_{i,j,k}^2 - (a_1 - a_2)^2}) \\ a_1 + f_{i,j,k} \end{cases}.$$

The three parts correspond to the following intervals, respectively

$$f_{i,j,k}^2 \geq (a_1 - a_3)^2 + (a_2 - a_3)^2,$$

$$(a_1 - a_2)^2 \leq f_{i,j,k}^2 < (a_1 - a_3)^2 + (a_2 - a_3)^2,$$

$$f_{i,j,k}^2 < (a_1 - a_2)^2.$$

To solve (A.8), which is not in analytical form, the fast Gauss-Seidel iteration with alternating sweeping orderings is used. For initialisation, the value of grid points on Γ is set to zero, and this value is fixed in later calculations. The rest of the points are set to large values, and these values will be updated later. The whole 3D grid is traversed in the following orders for the Gauss-Seidel iteration

- (1) $i = 1 : M, j = 1 : N, k = 1 : H$; (2) $i = M : 1, j = N : 1, k = H : 1$;
- (3) $i = M : 1, j = 1 : N, k = 1 : H$; (4) $i = 1 : M, j = N : 1, k = H : 1$;
- (5) $i = M : 1, j = N : 1, k = 1 : H$; (6) $i = 1 : M, j = 1 : N, k = H : 1$;
- (7) $i = 1 : M, j = N : 1, k = 1 : H$; (8) $i = M : 1, j = 1 : N, k = H : 1$.

References

- [1] D. Huang, E.A. Swanson, C.P. Lin, J.S. Schuman, W.G. Stinson, W. Chang, M.R. Hee, T. Flotte, K. Gregory, C.A. Puliafito, J.G. Fujimoto, Optical coherence tomography, Science 254 (5035) (1991) 1178–1181.
- [2] H. Ishikawa, D.M. Stein, G. Wollstein, S. Beaton, J.G. Fujimoto, J.S. Schuman, Macular segmentation with optical coherence tomography, Invest. Ophthalmol. Vis. Sci. 46 (6) (2005) 2012–2017.
- [3] M. Shahidi, Z. Wang, R. Zelkha, Quantitative thickness measurement of retinal layers imaged by optical coherence tomography, Am. J. Ophthalmol. 139 (6) (2005) 1056–1061.
- [4] D.C. Fernández, H.M. Salinas, C.A. Puliafito, Automated detection of retinal layer structures on optical coherence tomography images, Opt. Expr. 13 (25) (2005) 10200–10216.
- [5] M. Mayer, R. Tornow, R. Bock, J. Horngger, F. Kruse, Automatic nerve fiber layer segmentation and geometry correction on spectral domain OCT images using fuzzy c-means clustering, Invest. Ophthalmol. Vis. Sci. 49 (13) (2008) 1880.
- [6] A. Mishra, A. Wong, K. Bizheva, D.A. Clausi, Intra-retinal layer segmentation in optical coherence tomography images, Opt. Expr. 17 (26) (2009) 23719–23728.
- [7] A. Yazdanpanah, G. Hamarneh, B. Smith, M. Sarunic, Intra-retinal layer segmentation in optical coherence tomography using an active contour approach, in: Proceedings of the Medical Image Computing and Computer-Assisted Intervention – MICCAI 2009, Springer, 2009, pp. 649–656.
- [8] I. Ghorbel, F. Rossant, I. Bloch, S. Tick, M. Paques, Automated segmentation of macular layers in OCT images and quantitative evaluation of performances, Pattern Recognit. 44 (8) (2011) 1590–1603.
- [9] F. Rossant, I. Bloch, I. Ghorbel, M. Paques, Parallel double snakes. application to the segmentation of retinal layers in 2d-OCT for pathological subjects, Pattern Recognit. 48 (12) (2015) 3857–3870.
- [10] S.J. Chiu, X.T. Li, P. Nicholas, C.A. Toth, J.A. Izatt, S. Farsiu, Automatic segmentation of seven retinal layers in SDOCT images congruent with expert manual segmentation, Opt. Expr. 18 (18) (2010) 19413–19428.
- [11] Q. Yang, C.A. Reisman, Z. Wang, Y. Fukuma, M. Hangai, N. Yoshimura, A. Tomidokoro, M. Araie, A.S. Raza, D.C. Hood, et al., Automated layer segmentation of macular OCT images using dual-scale gradient information, Opt. Expr. 18 (20) (2010) 21293–21307.
- [12] X. Liu, J. Wang, Z. Yang, W. Hu, Automated segmentation of nine retinal layers with layer thickness information on SD-OCT images, in: Proceedings of the Eighth International Conference on Digital Image Processing (ICDIP 2016), International Society for Optics and Photonics, 2016, p. 10031G.

- [13] V. Kajić, B. Považay, B. Hermann, B. Hofer, D. Marshall, P.L. Rosin, W. Drexler, Robust segmentation of intraretinal layers in the normal human fovea using a novel statistical model based on texture and shape analysis, *Opt. Expr.* 18 (14) (2010) 14730–14744.
- [14] V. Kajić, M. Esmaelpour, B. Považay, D. Marshall, P.L. Rosin, W. Drexler, Automated choroidal segmentation of 1060 nm OCT in healthy and pathologic eyes using a statistical model, *Biomed. Opt. Express.* 3 (1) (2012) 86–103.
- [15] M. Pilch, Y. Wenner, E. Strohmayer, M. Preising, C. Friedburg, E.M. zu Bexten, B. Lorenz, K. Steiger, Automated segmentation of retinal blood vessels in spectral domain optical coherence tomography scans, *Biomed. Opt. Express.* 3 (7) (2012) 1478–1491.
- [16] J. Duan, C. Tench, I. Gottlob, F. Proudlock, L. Bai, Optical coherence tomography image segmentation, in: Proceedings of the IEEE International Conference on Image Processing (ICIP), IEEE, 2015, pp. 4278–4282.
- [17] M. Mujat, R.C. Chan, B. Cense, B.H. Park, C. Joo, T. Akkin, T.C. Chen, J.F. de Boer, Retinal nerve fiber layer thickness map determined from optical coherence tomography images, *Opt. Expr.* 13 (23) (2005) 9480–9491.
- [18] T.F. Cootes, C.J. Taylor, D.H. Cooper, J. Graham, Active shape models—their training and application, *Comput. Vis. Image Underst.* 61 (1) (1995) 38–59.
- [19] T.F. Cootes, G.J. Edwards, C.J. Taylor, Active appearance models, *IEEE Trans. Pattern Anal. Mach. Intell.* 6 (2001) 681–685.
- [20] M.K. Garvin, M.D. Abràmoff, X. Wu, S.R. Russell, T.L. Burns, M. Sonka, Automated 3-d intraretinal layer segmentation of macular spectral-domain optical coherence tomography images, *IEEE Trans. Med. Imaging* 28 (9) (2009) 1436–1447.
- [21] G. Quellec, K. Lee, M. Dolejsi, M.K. Garvin, M.D. Abràmoff, M. Sonka, Three-dimensional analysis of retinal layer texture: identification of fluid-filled regions in SD-OCT of the macula, *IEEE Trans. Med. Imaging* 29 (6) (2010) 1321–1330.
- [22] B.J. Antony, M.D. Abràmoff, M. Sonka, Y.H. Kwon, M.K. Garvin, Incorporation of texture-based features in optimal graph-theoretic approach with application to the 3d segmentation of intraretinal surfaces in SD-OCT volumes, in: Proceedings of the SPIE Medical Imaging, International Society for Optics and Photonics, 2012, p. 83141G.
- [23] P.A. Dufour, L. Ceklic, H. Abdillahi, S. Schroder, S. De Dzant, U. Wolf-Schnurbsch, J. Kowal, Graph-based multi-surface segmentation of OCT data using trained hard and soft constraints, *IEEE Trans. Med. Imaging* 32 (3) (2013) 531–543.
- [24] R. Kafieh, H. Rabbani, M.D. Abramoff, M. Sonka, Intra-retinal layer segmentation of 3d optical coherence tomography using coarse grained diffusion map, *Med. Image Anal.* 17 (8) (2013) 907–928.
- [25] J. Tian, B. Varga, G.M. Somfai, W.-H. Lee, W.E. Smiddy, D.C. DeBuc, Real-time automatic segmentation of optical coherence tomography volume data of the macular region, *PLoS ONE* 10 (8) (2015) e0133908.
- [26] J. Tian, B. Varga, E. Tatrai, P. Fanni, G.M. Somfai, W.E. Smiddy, D.C. DeBuc, Performance evaluation of automated segmentation software on optical coherence tomography volume data, *J. Biophotonics* 9 (5) (2016) 478–489.
- [27] K. Vermeer, J. Van der Schoot, H. Lemij, J. De Boer, Automated segmentation by pixel classification of retinal layers in ophthalmic OCT images, *Biomed. Opt. Express.* 2 (6) (2011) 1743–1756.
- [28] A.R. Fuller, R.J. Zawadzki, S. Choi, D.F. Wiley, J.S. Werner, B. Hamann, Segmentation of three-dimensional retinal image data, *IEEE Trans. Vis. Comput. Gr.* 13 (6) (2007) 1719–1726.
- [29] M. Szkulmowski, M. Wojtkowski, B. Sikorski, T. Bajraszewski, V.J. Srinivasan, A. Szkulmowska, J.J. Kalužny, J.G. Fujimoto, A. Kowalczyk, Analysis of posterior retinal layers in spectral optical coherence tomography images of the normal retina and retinal pathologies, *J. Biomed. Opt.* 12 (4) (2007) 041207.
- [30] A. Lang, A. Carass, M. Hauser, E.S. Sotirchos, P.A. Calabresi, H.S. Ying, J.L. Prince, Retinal layer segmentation of macular OCT images using boundary classification, *Biomed. Opt. Express.* 4 (7) (2013) 1133–1152.
- [31] H. Zhao, A fast sweeping method for Eikonal equations, *Math. Comput.* 74 (250) (2005) 603–627.
- [32] Y.-H. R. Tsai, L.-T. Cheng, S. Osher, H.-K. Zhao, Fast sweeping algorithms for a class of Hamilton-Jacobi equations, *SIAM J. Numer. Anal.* 41 (2) (2003) 673–694.
- [33] J. Duan, B. Haines, W.O. Ward, L. Bai, Surface reconstruction from point clouds using a novel variational model, in: *Research and Development in Intelligent Systems XXXII*, Springer, 2015, pp. 135–146.
- [34] D.C. DeBuc, A review of algorithms for segmentation of retinal image data using optical coherence tomography. *Image Segmentation*. InTech, 2011. DOI: 10.5772/15833.
- [35] Q. Song, X. Wu, Y. Liu, M. Sonka, M. Garvin, Simultaneous searching of globally optimal interacting surfaces with shape priors, in: *Proceedings of the IEEE Conference on Computer Vision and Pattern Recognition (CVPR)*, IEEE, 2010, pp. 2879–2886.
- [36] J. Duan, Z. Qiu, W. Lu, G. Wang, Z. Pan, L. Bai, An edge-weighted second order variational model for image decomposition, *Digit. Signal Process.* 49 (2016) 162–181.
- [37] J.A. Sethian, A fast marching level set method for monotonically advancing fronts, *Proc. Natl. Acad. Sci.* 93 (4) (1996) 1591–1595.
- [38] J.A. Sethian, *Level Set Methods and Fast Marching Methods: Evolving Interfaces in Computational Geometry, Fluid Mechanics, Computer Vision, and Materials Science*, 3, Cambridge University Press, 1999.
- [39] Y. Ding, M.C. Pardon, A. Agostini, H. Faas, J. Duan, W.O. Ward, F. Easton, D. Auer, L. Bai, Novel methods for microglia segmentation, feature extraction and classification, *IEEE/ACM Trans. Comput. Biol. Bioinf.* (2016), doi:10.1109/TCBB.2016.2591520.
- [40] D. Yang, G. Subramanian, J. Duan, S. Gao, L. Bai, R. Chandramohanadas, Y. Ai, A portable image-based cytometer for rapid malaria detection and quantification, *PLoS ONE* 12 (6) (2017) e0179161.
- [41] J. Duan, C. Tench, I. Gottlob, F. Proudlock, L. Bai, New variational image decomposition model for simultaneously denoising and segmenting optical coherence tomography images, *Phys. Med. Biol.* 60 (22) (2015) 8901.

Jinming Duan received his B.Sc. degree from the Nanjing University of Information Science and Technology, PR China, in 2011, and the M.Sc. degree from the Qingdao University, PR China, in 2014. He is currently a Ph.D. student with the School of Computer Science at the University of Nottingham, UK. His research interests include variational image restoration, multiphase image segmentation, implicit surface reconstruction and medical image analysis.

Christopher Tench received his B.Sc. (Hons) in Physics and Theoretical Physics from the University of Manchester, UK, in 1996. He received his Ph.D. in neuroimage analysis in 2003 from the University of Nottingham, UK while working as a research associate. Since then he has continued to work as a research fellow in the division of Clinical Neurology, at the University of Nottingham. His main research interests are applications of MRI to multiple sclerosis, including diffusion and spinal cord MRI.

Irene Gottlob is currently a professor leading the Leicester Ophthalmology group and her main areas of research are the regulation of eye movements and their disorders, in particular nystagmus. Current areas of active research include understanding the genetics of neuro-ophthalmic diseases, improving diagnosis and treatment of nystagmus, amblyopia and other neuro-ophthalmic diseases. Professor Gottlob is the section editor of the British Journal of Ophthalmology and on the editorial board of other scientific journals.

Frank Proudlock received his B.Sc. in Neuroscience at the University of Glasgow and his M.Sc. in Bioengineering at the University of Strathclyde, Glasgow. He received his Ph.D. at the University of Leicester in 2000 and has been a senior lecturer since 2014 where he has led investigations into visual system deficits in albinism, the impact of reading in nystagmus and the development of new treatments in visual system disease.

Li Bai is with the School of Computer Science, University of Nottingham. She has a B.Sc. and M.Sc. in Mathematics, and a Ph.D. in Computer Science from the University of Nottingham, UK. Her main research interests are in the area of computer vision, pattern recognition and medical image analysis.